Thermodynamic modelling of alkali-activated slag cements

Thermodynamic modelling of alkali-activated slag cements

Rupert J. Myers [1], Barbara Lothenbach [2], Susan A. Bernal [1], John L. Provis [1]*

[1] Department of Materials Science and Engineering, The University of Sheffield, Sir Robert Hadfield Building, Mappin St, Sheffield S1 3JD, UK

[2] Laboratory for Concrete and Construction Chemistry, EMPA, Dübendorf, 8600, Switzerland

* To whom correspondence should be addressed. Email j.provis@sheffield.ac.uk, phone +44 114 222 5490, fax +44 114 222 5493

Keywords

Thermodynamic modelling; alkali-activated slag cement; C-A-S-H; phase diagram; layered double hydroxide; zeolite

Abstract

This paper presents a thermodynamic modelling analysis of alkali-activated slag-based cements, which are high performance and potentially low-CO_2 binders relative to Portland cement. The

thermodynamic database used here contains a calcium (alkali) aluminosilicate hydrate ideal solid solution model (CNASH_ss), alkali carbonate and zeolite phases, and an ideal solid solution model for a hydrotalcite-like Mg-Al layered double hydroxide phase. Simulated phase diagrams for NaOH- and Na_2SiO_3-activated slag-based cements demonstrate the high stability of zeolites and other solid phases in these materials. Thermodynamic modelling provides a good description of the chemical compositions and types of phases formed in Na_2SiO_3-activated slag cements over the most relevant bulk chemical composition range for these cements, and the simulated volumetric properties of the cement paste are consistent with previously measured and estimated values. Experimentally determined and simulated solid phase assemblages for Na_2CO_3-activated slag cements were also found to be in good agreement. These results can be used to design the chemistry of alkali-activated slag-based cements, to further promote the uptake of this technology and valorisation of metallurgical slags.

1. Introduction

Development of high performance and low CO_2 cement-based materials is needed to reduce the CO_2 footprint of the construction industry. Alkali-activated cements are formed through the reaction of a soluble alkali source (the 'activator'), water and aluminosilicate precursors, which are often sourced as industrial by-products (Provis, 2014). Blast furnace slag is one such material, and forms an important component of many modern cements, including use as the main raw material in production of alkali-activated slag (AAS) cements (Provis and Bernal, 2014). The reactive component of blast furnace slag is a calcium-magnesium aluminosilicate glass that dissolves under the high pH conditions provided by the activator to form a hydrated phase assemblage that consolidates into a hardened binder. AAS-based cements are attractive solutions for waste valorisation and utilisation of industrial by-products, e.g. in immobilisation matrices for radioactive wastes (Bai et al., 2011), and can provide substantial CO_2 savings relative to Portland cement (PC)-based materials (McLellan et al., 2011).

Understanding the durability of alkali-activated cements is a key scientific challenge facing their commercial uptake and utilisation (van Deventer et al., 2012). Durability is intimately linked to the chemistry and microstructure of these cements, and thus depends on physicochemical factors including chemical shrinkage and the solid phase assemblage formed.

The main component of hardened AAS-based materials is a calcium (alkali) aluminosilicate hydrate (C-(N-)A-S-H) gel [1] that is poorer in Ca (molar Ca/Si ratio ≈ 1 (Shi et al., 2006)) and richer in Al (molar Al/Si ratio > 0.1 (Le Saoût et al., 2011; Myers et al., 2013; Richardson et al., 1994)) than the calcium (alumino)silicate hydrate (C-(A-)S-H) gel formed in hydrated PC (Taylor et al., 2010). The solid phase assemblage in AAS cements contains phases other than C-(N-)A-S-H gel, typically including Mg-Al layered double hydroxide (LDH) phases (Richardson et al., 1994; Wang and Scrivener, 1995) and aluminoferrite-mono (AFm) type phases including strätlingite (C_2ASH_8) (Ben Haha et al., 2012; Richardson et al., 1994; Wang and Scrivener, 1995), and calcium monocarboaluminate hydrate ($C_4A\underline{c}H_{11}$) in Na_2CO_3 (N$\underline{c}$)-activated slag (N$\underline{c}$-AS) cement (Shi et al., 2006). Katoite (C_3AH_6) (Bonk et al., 2003), zeolites including gismondine and heulandite (Bernal et al., 2015; Bernal et al., 2011), and the third aluminate hydrate (TAH) (Myers et al., 2015a), which is described as a poorly ordered $Al(OH)_3$ phase (Taylor et al., 2010), may additionally form in AAS cements. Recently, evidence for the formation of alkali aluminosilicate (hydrate) (N-A-S(-H)) gels in AAS cement has been presented (Myers et al., 2015a; Myers et al., 2013); this phase is considered to be similar to the 'geopolymer' gels formed through alkali-activation of low-Ca raw materials (Provis et al., 2005).

Thermodynamic modelling can be used to predict the chemistry of hydrated/alkali-activated cements, assuming equilibrium between the solid reaction products and pore solution (Atkins et al., 1992; Lothenbach, 2010; Savage et al., 2011), which is critically important in understanding their long-term behaviour, e.g. in radioactive waste disposal applications (Glasser and Atkins, 1994). This approach

[1] The various alkalis that may be incorporated into C-(N-)A-S-H gel are all represented by Na here because the alkali source in an alkali-activated cement is typically Na-based. Cement chemistry notation is used throughout the text: C = CaO; S = SiO_2; A = Al_2O_3; N = Na_2O; H = H_2O; M = MgO; $\underline{c}$ = CO_2; and $\underline{s}$ = SO_3.

has been applied to AAS cements in the past (Lothenbach and Gruskovnjak, 2007), however the calcium silicate hydrate (C-S-H) thermodynamic model (Kulik and Kersten, 2001) used in that study does not explicitly define the uptake of Al and Na which is needed to fully describe C-(N-)A-S-H gel. Chemically complete definitions of Al chemistry in the thermodynamic models used to simulate the phases formed in AAS-based cements are important in enabling accurate prediction of the chemistry of these cements. The inclusion of alkalis as a key component in thermodynamic models for C-(N-)A-S-H gel is also important to enable correct description of the solubility relationships of this phase under the high pH conditions (>12) and alkali concentrations (tens to hundreds of mmol/L) relevant to the majority of cementitious materials (Myers et al., 2014).

The CNASH_ss thermodynamic model used in the current paper was recently developed (Myers et al., 2014) to formally account for Na and tetrahedral Al incorporated in Ca/Si < 1.3 C-(N-)A-S-H gel. Here, this thermodynamic model is used to simulate the chemistry of AAS cements activated by aqueous solutions of NaOH ($(NH)_{0.5}$), Na_2SiO_3 (NS), $Na_2Si_2O_5$ (NS_2) and Nc. This thermodynamic model can describe a large set of solubility data for the CaO-(Na_2O,Al_2O_3)-SiO_2-H_2O and AAS cement systems, and closely matches the published chemical compositions of calcium aluminosilicate hydrate (C-A-S-H) gel, and the volumetric properties of C-(N-)A-S-H gel measured in a sodium silicate-activated slag cement (Myers et al., 2014). The CNASH_ss thermodynamic model is assessed here in terms of the prediction of solid phase assemblages and the Al content of C-(N-)A-S-H gel over the bulk slag chemical composition range which is most relevant to AAS cement-based materials. These simulations are performed using the Gibbs energy minimisation software GEM-Selektor v.3 (http://gems.web.psi.ch/) (Kulik et al., 2013; Wagner et al., 2012) and an expanded thermodynamic database for cements, based on the CEMDATA07 database (Babushkin et al., 1985; Hummel et al., 2002; Lothenbach et al., 2008; Lothenbach and Winnefeld, 2006; Matschei et al., 2007; Möschner et al., 2008; Möschner et al., 2009; Schmidt et al., 2008; Thoenen and Kulik, 2003) with the addition of an updated definition of Mg-Al LDH intercalated with OH^- (MA-OH-LDH), and including some zeolites and alkali carbonates. The results are discussed in terms of implications for the design of high performance AAS-based cements.

2. Methods

2.1 Thermodynamic model for C-(N-)A-S-H gel

The CNASH_ss thermodynamic model (Myers et al., 2014) is formulated as an ideal solid solution with mixing on six of eight sublattice sites to give three C-S-H gel end-members, one calcium (alkali) silicate hydrate (C-(N-)S-H) gel end-member, two C-A-S-H gel end-members and two C-(N-)A-S-H gel end-members (Table 1). End-member chemical compositions are defined in this model by extension of the 'Substituted General Model' (Richardson and Groves, 1993) for consistency with tobermorite-like nanostructures containing no 'interstratified $Ca(OH)_2$' (Richardson, 2004), which limits the applicability of the CNASH_ss thermodynamic model to Ca/Si ratios <1.3 in the C-(N-)A-S-H gel. Pentahedral Al (Al[5]) and octahedral Al (Al[6]) are not explicitly considered in the end-member structures described by CNASH_ss.

C-(N-)A-S-H gel is formally described in terms of non-cross-linked chain structures in the CNASH_ss thermodynamic model, but without precluding representation of cross-linked tobermorite-like chain structures, because these structural types cannot be differentiated by bulk chemical composition alone. Thermodynamic calculations using the CNASH_ss thermodynamic model are therefore also consistent with cross-linked C-(N-)A-S-H gel structural models such as those described by the 'Cross-linked Substituted Tobermorite Model' (CSTM) (Myers et al., 2013). Full details of the development and implementation of the CNASH_ss thermodynamic model are given in (Myers et al., 2014).

2.2 Thermodynamic model for MA-OH-LDH

Thermodynamic data for MA-OH-LDH were reformulated into an ideal solid solution thermodynamic model (MA-OH-LDH_ss) containing three end-members with Mg/Al ratios of 2, 3 and 4 (Table 1) to

match the known chemical composition range of this solid solution ($Mg_{(1-x)}Al_x(OH)_{(2+x)}\cdot mH_2O$, $0.2 \leq x \leq 0.33$ (Richardson, 2013)).

Recalculation of recently published solubility data for Mg/Al = 2 MA-OH-LDH (M_4AH_{10}) (Gao and Li, 2012) and existing solubility data for this phase (Bennett et al., 1992) was performed in GEM-Selektor v.3 (http://gems.web.psi.ch/) (Kulik et al., 2013; Wagner et al., 2012) using the dissolution reaction eq.(1):

$$Mg_4Al_2(OH)_{14}\cdot 3H_2O \rightleftharpoons^{K_s} 4Mg^{2+} + 2AlO_2^- + 6(OH)^- + 7H_2O \quad (1)$$

where K_s is the solubility product. Solubility data for this phase were also calculated using the additivity method (Anderson and Crerar, 1993) with brucite ($Mg(OH)_{2\ (s)}$), magnesite ($MgCO_{3\ (s)}$) (Table 1), and hydrotalcite ($Mg_{0.74}Al_{0.26}(OH)_2(CO_3)_{0.13}\cdot 0.39H_2O_{\ (s)}$) (Allada et al., 2005) constituents.

The recalculation results indicate that the solubility product used previously by Lothenbach and Winnefeld (2006) to describe this phase ($\log_{10}(K_s)$ = -56.02 at 25°C and 1 bar), taken from the low solubility data reported by Bennett et al. (1992), is not consistent with the solubility data reported by Gao and Li (Gao and Li, 2012) (Figure 1). Here, a solubility product of $\log_{10}(K_s)$ = -49.70 at 25°C and 1 bar is selected for improved consistency with the solubility data reported by Gao and Li (Gao and Li, 2012). The standard heat capacity and entropy of this phase are adapted from the thermodynamic data reported by Allada et al. (Allada et al., 2005) for $Mg_{0.74}Al_{0.26}(OH)_2(CO_3)_{0.13}.0.39H_2O$ using the additivity method with $Mg(OH)_{2\ (s)}$ and $MgCO_{3\ (s)}$ constituents, i.e. the standard heat capacity for M_4AH_{10} is calculated via eq.(2):

$$Cp^o_{M_4AH_{10}} = 2\left(\tfrac{1}{0.26}Cp^o_{Mg_{0.74}Al_{0.26}(OH)_2(CO_3)_{0.13}\cdot 0.39H_2O} - 0.5Cp^o_{MgCO_3} - 0.346Cp^o_{Mg(OH)_2}\right) \quad (2)$$

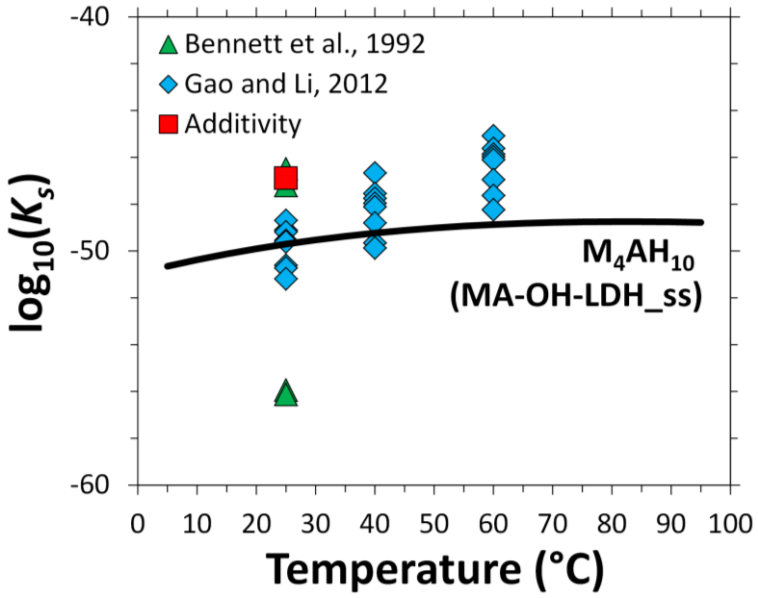

Figure 1. Comparison between the recalculated solubility data (Bennett et al., 1992; Gao and Li, 2012), results using the additivity method, and calculated solubility of the M_4AH_{10} end-member of the MA-OH-LDH_ss thermodynamic model used in this work (thick black line) (P = 1 bar). The green triangles at $\log_{10}(K_s)$ = -56.02 (25°C and 1 bar), represents the solubility product used previously to describe this phase in the cement chemistry literature.

Standard entropies and heat capacities for Mg/Al = 3 MA-OH-LDH (M_6AH_{12}) and Mg/Al = 4 MA-OH-LDH (M_8AH_{14}) were determined in the same manner (using solid constituents and a reaction analogous to eq.(2)), using the thermodynamic data reported by Allada et al. (Allada et al., 2005). A difference of -22.32 $\log_{10}$ units was specified between the solubility products of M_4AH_{10} ($\log_{10}(K_s)$ = -49.70) and M_6AH_{12} ($\log_{10}(K_s)$ = -72.02), and between those of M_6AH_{12} and M_8AH_{14} ($\log_{10}(K_s)$ = -94.34) at 25°C and 1 bar, which is the difference between the solubility products of these phases when determined using the additivity method described here. A similar difference is found between reported thermodynamic data for MA-c-LDH ($Mg_4Al_2(OH)_{12}(CO_3).4H_2O$, $\log_{10}(K_s)$ = -44.19 (Rozov et al., 2011) and $Mg_6Al_2(OH)_{16}(CO_3).5H_2O$, $\log_{10}(K_s)$ = -66.58 (Rozov, 2010)), which suggests that the additivity approach is appropriate for these structurally-similar Mg-Al LDH phases. The three MA-OH-LDH phases M_4AH_{10}, M_6AH_{12} and M_8AH_{14} were specified as end-members of the ideal solid solution 'MA-OH-LDH_ss'. This is justified because it has been shown that the assumption of mechanical (ideal) mixing is appropriate for modelling the total solubility of the structurally-similar hydrotalcite-pyroaurite solid solution series (Rozov et al., 2011). This MA-OH-LDH solid solution model is used in the thermodynamic modelling performed in this work.

2.3 Occurrence of Mg, Fe and S-bearing phases

Thermodynamic modelling of AAS cements requires consideration of additional constituent elements outside the CaO-Na_2O-Al_2O_3-SiO_2-H_2O system, most notably Mg, Fe and S, as well as carbonates. While the precipitation of Mg in AAS cement is generally well explained by its incorporation into Mg-Al LDH phases (Ben Haha et al., 2011b; Richardson et al., 1994; Wang and Scrivener, 1995), there is less consensus regarding the precipitation of Fe and S. Fe was excluded from this work, consistent with the passivated state of this element in GBFS (Bernal et al., 2014a), and S released by the slag was represented as S^{2-} with its oxidation limited by using a simulated $N_{2\,(g)}$ atmosphere in the thermodynamic modelling calculations.

2.4 Other solid phases

Thermodynamic data for cement-related solid phases other than C-(N-)A-S-H gel and MA-OH-LDH were taken from the PSI/Nagra 12/07 thermodynamic database (Thoenen et al., 2013) and the CEMDATA07 thermodynamic database, which was updated to include recently published data for $Al(OH)_3$ and hydrogarnet phases (Dilnesa et al., 2014; Lothenbach et al., 2012) (Table 1).

197 Table 1. Thermodynamic properties of solid phases at 298.15 K and 1 bar.

Phases [a]	$V°$ (cm^3 mol^{-1})	$\Delta H_f°$ (kJ mol^{-1})	$\Delta G_f°$ (kJ mol^{-1})	$S°$ (J mol^{-1} K^{-1})	$Cp°$ (J mol^{-1} K^{-1})	Reference
½AH_3 (microcrystalline)	32.0	-1265	-1148	140	93.1	(Lothenbach et al., 2012)
Portlandite, CH	33.1	-985	-897	83.4	87.5	(Robie and Hemingway, 1995)
SiO_2 (amorphous)	29.0	-903	-849	41.3	44.5	(Helgeson et al., 1978; Kulik and Kersten, 2001)
C_2AH_8	90.1	-5278	-4696	450	521	(Lothenbach et al., 2012)
Katoite, (C_3AH_6)	150	-5537	-5008	422	446	(Lothenbach et al., 2012)
C_4AH_{19}	382	-1002	-8750	1120	1382	(Lothenbach et al., 2012)
CAH_{10}	194	-5288	-4623	610	668	(Lothenbach et al., 2012)
Strätlingite, C_2ASH_8	216	-6360	-5705	546	603	(Matschei et al., 2007)
Calcium monocarboaluminate hydrate, $C_4A\underline{c}H_{11}$	262	-8250	-7337	657	881	(Matschei et al., 2007)
Calcium hemicarboaluminate hydrate, $C_4A\underline{c}_{0.5}H_{12}$	285	-8270	-7336	713	906	(Matschei et al., 2007)
Calcium tricarboaluminate hydrate, $C_6A\underline{c}_3H_{32}$	650	-16792	-14566	1858	2121	(Matschei et al., 2007)
Ettringite, $C_6A\underline{s}_3H_{32}$	707	-17535	-15206	1900	2174	(Lothenbach et al., 2008)
Gypsum, $C\underline{s}H_2$	74.7	-2023	-1798	194	186	(Hummel et al., 2002; Thoenen et al., 2013)
Anhydrite, $C\underline{s}$	45.9	-1435	-1322	107	99.6	(Hummel et al., 2002; Thoenen et al., 2013)
Lime, C	16.8	-635	-604	39.7	42.8	(Helgeson et al., 1978)
Brucite, MH	24.6	-923	-832	63.1	77.3	(Helgeson et al., 1978; Hummel et al., 2002; Thoenen et al., 2013)
MA-$\underline{c}$-LDH, $M_4A\underline{c}H_9$	220	-7374	-6580	551	647	(Lothenbach et al., 2008)
C-(N-)A-S-H gel ideal solid solution end-members, 'CNASH_ss' (Myers et al., 2014)						
5CA, $C_{1.25}A_{0.125}S_1H_{1.625}$	57.3	-2491	-2293	163	177	(Myers et al., 2014)
INFCA, $C_1A_{0.15625}S_{1.1875}H_{1.65625}$	59.3	-2551	-2343	154	181	(Myers et al., 2014)
5CNA, $C_{1.25}N_{0.25}A_{0.125}S_1H_{1.375}$	64.5	-2569	-2382	195	176	(Myers et al., 2014)
INFCNA, $C_1N_{0.34375}A_{0.15625}S_{1.1875}H_{1.3125}$	69.3	-2667	-2474	198	180	(Myers et al., 2014)
INFCN, $C_1N_{0.3125}S_{1.5}H_{1.1875}$	71.1	-2642	-2452	186	184	(Myers et al., 2014)
T2C*, $C_{1.5}S_1H_{2.5}$ [b]	80.6	-2721	-2465	167	237	(Myers et al., 2014)
T5C*, $C_{1.25}S_{1.25}H_{2.5}$ [b]	79.3	-2780	-2517	160	234	(Myers et al.,

						2014)
TobH*, $C_1S_{1.5}H_{2.5}$ [b]	85.0	-2831	-2560	153	231	(Myers et al., 2014)
Calcium monosulfoaluminate-hydroxoaluminate hydrate non-ideal solid solution (Matschei et al., 2007)						
Calcium monosulfoaluminate hydrate, $C_4A\underline{S}H_{12}$	309	-8750	-7779	821	942	(Matschei et al., 2007)
C_4AH_{13}	274	-8300	-7324	700	930	(Lothenbach et al., 2012)
MA-OH-LDH ideal solid solution end-members, 'MA-OH-LDH_ss'						
M_4AH_{10}	219	-7160	-6358	549	648	(Allada et al., 2005; Richardson, 2013)
M_6AH_{12}	305	-9007	-8023	675	803	This study [c]
M_8AH_{14}	392	-10853	-9687	801	958	This study [c]
Carbonates						
Aragonite, $C\underline{c}$	34.2	-1207	-1128	90.2	81.3	(Hummel et al., 2002; Thoenen et al., 2013)
Calcite, $C\underline{c}$	36.9	-1207	-1129	92.7	81.9	(Hummel et al., 2002; Thoenen et al., 2013)
Dolomite (disordered), $CM\underline{c}_2$	64.4	-2317	-2157	167	158	(Hummel et al., 2002; Thoenen et al., 2013)
Natron, $N\underline{c}H_{10}$	197	-4079	-3428	563	550	(Königsberger et al., 1999; Taga, 1969)
Gaylussite, $NC\underline{c}_2H_5$	149	-3834	-3372	387	- [d]	(Dickens and Brown, 1969; Königsberger et al., 1999)
Pirssonite, $NC\underline{c}_2H_2$	104	-2956	-2658	239	329	(Dickens and Brown, 1969; Königsberger et al., 1999)
Magnesite, $M\underline{c}$	28.0	-1113	-1029	65.7	75.8	(Hummel et al., 2002; Thoenen et al., 2013)
Huntite, $CM_3\underline{c}_4$	123	-4533	-4206	300	310	(Graf and Bradley, 1962; Hemingway and Robie, 1972; Königsberger et al., 1999)
Artinite, $M_2\underline{c}H_4$	96.2	-2921	-2568	233	248	(de Wolff, 1952; Hemingway and Robie, 1972; Königsberger et al., 1999)
Lansfordite, $M\underline{c}H_5$	103	-2574	-2198	250	386	(Hill et al., 1982; Königsberger et al., 1999)
Zeolites						
Na-analcime, $\|Na_{0.32}\|.[Al_{0.32}Si_{0.68}O_2].0.333H_2O$	32.5 [c]	-1099	-1026	75.6	70.5	(Johnson et al., 1982)

Natrolite, $\|Na_{0.4}\|.[Al_{0.4}Si_{0.6}O_2].0.4H_2O$	33.8 [c]	-1144	-1063	71.9	60.4	(Johnson et al., 1983)
Ca-heulandite, $\|Ca_{0.111}\|.[Al_{0.222}Si_{0.778}O_2].0.667H_2O$	35.2 [e]	-1179	-1090	87.1	82.9	(Kiseleva et al., 2001)
(Ca,Na)-heulandite, $\|Ca_{0.111}Na_{0.028}\|.[Al_{0.25}Si_{0.75}O_2].0.667H_2O$	35.2 [e]	-1185	-1094	84.0	82.9	(Kiseleva et al., 2001)
Basic sodalite, $\|Na_{0.65}(OH)_{0.15}\|.[Al_{0.5}Si_{0.5}O_2].0.27H_2O$	35.0 [e]	-1190	-1106	67.8 [f]	66.7 [f]	(Moloy et al., 2006)

[a] Cement chemistry notation is used: C = CaO; S = SiO_2; A = Al_2O_3; H = H_2O; N = Na_2O; M = MgO; $\underline{c}$ = CO_2; $\underline{s}$ = SO_3.

[b] The asterisks for the T2C*, T5C* and TobH* end-members indicate that these components have slightly modified thermodynamic properties but the same chemical composition relative to the T2C, T5C and TobH end-members of the downscaled CSH3T thermodynamic model (Kulik, 2011).

[c] Thermodynamic properties based on the thermochemical data in (Allada et al., 2005) and solubility data in (Bennett et al., 1992; Gao and Li, 2012), section 2.2, with molar volumes calculated from (Richardson, 2013).

[d] Not available

[e] Molar volumes calculated from framework densities, lattice types and lattice cell parameters for each zeolite framework type (Baerlocher et al., 2007).

[f] Standard entropy and heat capacity estimated using the additivity method (Anderson and Crerar, 1993) based on $H_2O_{(l)}$ (Table 2), gibbsite (Helgeson et al., 1978; Hummel et al., 2002), $NaOH_{(s)}$ (Robie and Hemingway, 1995) and amorphous SiO_2 (Table 1).

Thermodynamic data for some zeolites and alkali carbonate minerals were used to provide a preliminary assessment of the stability of these phases in AAS cements (Table 1) and should be treated as provisional only, because the thermodynamic data were not recompiled for full internal consistency with the Nagra-PSI and CEMDATA07 thermodynamic databases. Reliable thermodynamic data for other Na-carbonates which can form in AAS cements (i.e. natrite, thermonatrite, nahcolite and trona) were not available (Königsberger et al., 1999; Monnin and Schott, 1984), and so were not included in the simulations.

The formation of siliceous hydrogarnet was suppressed in the simulations because this phase does not tend to form at ambient temperature and pressure, possibly for kinetic reasons (Lothenbach et al., 2008). No additional restrictions related to the formation of any other solid phases shown in Table 1 were specified.

2.5 Approach

Thermodynamic modelling was performed using the Gibbs energy minimisation software GEM-Selektor v.3 (http://gems.web.psi.ch/) (Kulik et al., 2013; Wagner et al., 2012), with thermodynamic data for the solid phases shown in Table 1 and thermodynamic data for aqueous species/complexes and gases shown in Tables 2 and 3, respectively. The Truesdell-Jones form of the extended Debye-Hückel equation (eq.(3)) (Helgeson et al., 1981) and the ideal gas equation of state were used for the aqueous and gaseous phase models, respectively, with the average ion size ($\dot{a}$, Å) and the parameter for common short-range interactions of charged species (b_γ, kg mol^{-1}) specified to represent NaOH-dominated solutions (3.31 Å and 0.098 kg mol^{-1}, respectively (Helgeson et al., 1981)).

$$\log_{10}\gamma_j = \frac{-A_\gamma z_j^2\sqrt{I}}{1+\dot{a}B_\gamma\sqrt{I}} + b_\gamma I + \log_{10}\frac{x_{jw}}{X_w} \quad (3)$$

The parameters γ_j and z_j in eq.(3) are the activity coefficient and charge of the j^{th} aqueous species, respectively, A_γ (kg$^{0.5}$ mol$^{-0.5}$) and B_γ (kg$^{0.5}$ mol$^{-0.5}$ cm^{-1}) are T,P-dependent electrostatic parameters, I is the ionic strength of the aqueous electrolyte phase (mol kg^{-1}), x_{jw} (mol) is the molar quantity of water and X_w (mol) is the total molar amount of the aqueous phase. The activity of water is calculated from the osmotic coefficient (Helgeson et al., 1981) and unity activity coefficients for neutral dissolved species are used.

Table 2. Thermodynamic properties of the aqueous species used in the thermodynamic modelling simulations.

Species/complex [a]	$V°$ (cm^3 mol^{-1})	$\Delta H_f°$ (kJ mol^{-1})	$\Delta G_f°$ (kJ mol^{-1})	$S°$ (J mol^{-1} K^{-1})	$Cp°$ (J mol^{-1} K^{-1})	Reference
Al^{3+}	-45.2	-530.6	-483.7	-325.1	-128.7	(Shock et al., 1997)
AlO^+ (+ H_2O = $Al(OH)_2^+$)	0.3	-713.6	-660.4	-113	-125.1	(Shock et al., 1997)
AlO_2^- (+ $2H_2O$ = $Al(OH)_4^-$)	9.5	-925.6	-827.5	-30.2	-49	(Shock et al., 1997)
$AlOOH^o$ (+ $2H_2O$ = $Al(OH)_3^o$)	13	-947.1	-864.3	20.9	-209.2	(Shock et al., 1997)
$AlOH^{2+}$	-2.7	-767.3	-692.6	-184.9	56	(Shock et al.,

						1997)
$AlHSiO_3^{2+}$ (+ H_2O = $AlSiO(OH)_3^{2+}$)	-40.7	-1718	-1541	-304.2	-215.9	(Matschei et al., 2007)
$AlSiO_4^-$ (+ $3H_2O$ = $AlSiO(OH)_6^-$)	25.5	-1834	-1681	11.1	-4.6	(Matschei et al., 2007)
$AlSO_4^+$	-6.0	-1423	-1250	-172.4	-204.0	(Matschei et al., 2007)
$Al(SO_4)_2^-$	31.1	-2338	-2006	-135.5	-268.4	(Matschei et al., 2007)
Ca^{2+}	-18.4	-543.1	-552.8	-56.5	-30.9	(Shock et al., 1997)
$CaOH^+$	5.8	-751.6	-717	28	6	(Shock et al., 1997)
$CaHSiO_3^+$ (+ H_2O = $CaSiO(OH)_3^+$)	-6.7	-1687	-1574	-8.3	137.8	(Sverjensky et al., 1997)
$CaSiO_3^o$ (+ H_2O = $CaSiO_2(OH)_2^o$)	15.7	-1668	-1518	-136.7	88.9	(Matschei et al., 2007)
$CaSO_4^o$	4.7	-1448	-1310	20.9	-104.6	(Sverjensky et al., 1997)
$CaCO_3^o$	-1.6	-1202	-1099	10.5	-123.9	(Sverjensky et al., 1997)
$CaHCO_3^+$	13.3	-1232	-1146	66.9	233.7	(Hummel et al., 2002; Thoenen et al., 2013)
K^+	9.0	-252.1	-282.5	101	8.4	(Shock et al., 1997)
KOH^o	15	-474.1	-437.1	108.4	-85	(Shock et al., 1997)
KSO_4^-	27.5	-1159	-1032	146.4	-45.1	(Sverjensky et al., 1997)
Na^+	-1.2	-240.3	-261.9	58.4	38.1	(Shock et al., 1997)
$NaOH^o$	3.5	-470.1	-418.1	44.8	-13.4	(Shock et al., 1997)
$NaSO_4^-$	18.6	-1147	-1010	101.8	-30.1	(Matschei et al., 2007)
$NaCO_3^-$	-0.4	-938.6	-797.1	-44.3	-51.3	(Hummel et al., 2002; Thoenen et al., 2013)
$NaHCO_3^o$	32.3	-929.5	-847.4	154.7	200.3	(Hummel et al., 2002; Thoenen et al., 2013)
$HSiO_3^-$ (+ H_2O = $SiO(OH)_3^-$)	4.5	-1145	-1014	20.9	-87.2	(Sverjensky et al., 1997)
SiO_2^o (+ $2H_2O$ = $Si(OH)_4^o$)	16.1	-887.9	-833.4	41.3	44.5	(Kulik and Kersten, 2001; Shock et al., 1989)
SiO_3^{2-} (+ H_2O = $SiO_2(OH)_2^{2-}$)	34.1	-1099	-938.5	-80.2	119.8	(Matschei et al., 2007)
$S_2O_3^{2-}$	27.6	-649.9	-520.0	66.9	-238.5	(Shock et al., 1997)
HSO_3^-	33.0	-627.7	-529.1	139.7	-5.4	(Shock et al., 1997)
SO_3^{2-}	-4.1	-636.9	-487.9	-29.3	-281.0	(Shock et al.,

						1997)
HSO_4^-	34.8	-889.2	-755.8	125.5	22.7	(Shock et al., 1997)
SO_4^{2-}	12.9	-909.7	-744.5	18.8	-266.1	(Shock et al., 1997)
H_2S^o	35.0	-39.0	-27.9	125.5	179.2	(Shock et al., 1997)
HS^-	20.2	-16.2	12.0	68.2	-93.9	(Shock et al., 1997)
S^{2-}	20.2	92.2	120.4	68.2	-93.9	(Shock et al., 1997)
Mg^{2+}	-22.0	-465.9	-454.0	-138.1	-21.7	(Shock et al., 1997)
$MgOH^+$	1.6	-690.0	-625.9	-79.9	129.2	(Shock et al., 1997)
$MgHSiO_3^+$ (+ H_2O = $MgSiO(OH)_3^+$)	-10.9	-1614	-1477	-99.5	158.6	(Shock et al., 1997)
$MgSO_4^o$	1.8	-1369	-1212	-50.9	-90.3	(Hummel et al., 2002; Shock et al., 1997; Thoenen et al., 2013)
$MgSiO_3^o$ (+ H_2O = $MgSiO_2(OH)_2^o$)	12.1	-1597	-1425	-218.3	98.2	(Hummel et al., 2002; Thoenen et al., 2013)
$MgCO_3^o$	-16.7	-1132	-999.0	-100.4	-116.5	(Hummel et al., 2002; Sverjensky et al., 1997; Thoenen et al., 2013)
$MgHCO_3^+$	9.3	-1154.0	-1047	-12.6	254.4	(Hummel et al., 2002; Thoenen et al., 2013)
CO_2^o	32.8	-413.8	-386.0	117.6	243.1	(Hummel et al., 2002; Shock et al., 1989; Thoenen et al., 2013)
CO_3^{2-}	-6.1	-675.3	-528.0	-50.0	-289.3	(Shock et al., 1997)
HCO_3^-	24.2	-690.0	-586.9	98.5	-34.8	(Shock et al., 1997)
CH_4^o	37.4	-87.8	-34.4	87.8	277.3	(Hummel et al., 2002; Shock and Helgeson, 1990; Thoenen et al., 2013)
OH^-	-4.7	-230	-157.3	-10.7	-136.3	(Shock et al., 1997)
H^+	0	0	0	0	0	(Shock et al., 1997)
H_2O^o	18.1	-285.9	-237.2	69.9	75.4	(Johnson et al., 1992)
H_2^o	25.3	-4.0	17.7	57.7	166.9	(Hummel et al.,

						2002; Shock et al., 1989; Thoenen et al., 2013)
N_2^o	33.4	-10.4	18.2	95.8	234.2	(Shock et al., 1989)
O_2^o	30.5	-12.2	16.4	109	234.1	(Shock et al., 1989)

[a] The hydration reactions shown in parentheses indicate hydrated species/complexes represented by the simulated aqueous species/complexes.

Table 3. Thermodynamic properties of the gases used in the thermodynamic modelling simulations.

Gases	$V°$ **(cm^3 mol^{-1})**	$\Delta H_f°$ **(kJ mol^{-1})**	$\Delta G_f°$ **(kJ mol^{-1})**	$S°$ **(J mol^{-1} K^{-1})**	$Cp°$ **(J mol^{-1} K^{-1})**	**Reference**
N_2	24790	0	0	191.6	29.1	(Wagman et al., 1982)
O_2	24790	0	0	205.1	29.3	(Wagman et al., 1982)
H_2	24790	0	0	130.7	28.8	(Wagman et al., 1982)
CO_2	24790	-393.5	-394.4	213.7	37.1	(Wagman et al., 1982)
CH_4	24790	-74.8	-50.7	186.2	35.7	(Wagman et al., 1982)
H_2S	24790	-20.6	-33.8	205.8	34.2	(Wagman et al., 1982)

Chemical equilibrium between the solid, aqueous and gaseous phases was assumed, and the simulated slag was specified to dissolve congruently at each particular bulk slag chemical composition. The assumption of congruent dissolution is valid for calcium aluminosilicate glasses of similar bulk chemical compositions to GBFS in highly under-saturated conditions at pH = 13 (Snellings, 2013). This condition is likely to be approximated in AAS cements when the solution pH is sufficiently high (Bernal et al., 2015), although it is clear that this assumption will need to be revisited in some systems, particularly for AAS cements cured for long times or synthesised with less basic activators such as N<u>c</u> (Bernal et al., 2015).

Simulations of AAS cements were performed using 100 g slag, additions of H_2O, NaOH or Na_2O, SiO_2 and Na_2CO_3 to achieve fixed water to binder (w/b, where binder = slag + anhydrous activator

component) ratios of 0.4 and activator concentrations of 4 g Na_2O equivalent/100 g slag (the activators used are NaOH, Na_2SiO_3, $Na_2Si_2O_5$ and Na_2CO_3), a nitrogen atmosphere (10 mol $N_{2\,(g)}$ per 100 g slag), and temperature/pressure conditions of 298.15 K and 1 bar. This simulation setup directly represents the AAS cements studied in (Bernal et al., 2015; Bernal et al., 2014b; Myers et al., 2015a; Myers et al., 2013), and is also similar to the AAS cement formulations reported in (Ben Haha et al., 2011b, 2012; Le Saoût et al., 2011) (which had ~3 mass% Na_2O equivalent and w/b = 0.4). With the exception of the phase diagram simulations (section 3.4), the simulated slag compositions are based on the GBFS composition shown in Table 4.

Table 4. Bulk chemical composition of the GBFS (from (Myers et al., 2015a)) used to specify the chemical compositions of the simulated slag in the thermodynamic modelling simulations.

Component	Chemical composition (mass%)
SiO_2	33.8
CaO	42.6
MgO	5.3
Al_2O_3	13.7
Na_2O	0.1
K_2O	0.4
SO_3 [a]	0.8
Other	1.5
LOI [b]	1.8
Total	100

[a] S is represented in oxide form in standard XRF analysis, but S is treated as S^{2-} here (see section 2.2).
[b] LOI is loss on ignition at 1000°C.

In section 3.1, the utility of the thermodynamic database (Tables 1-3) is assessed by using the slag composition given in Table 4 in terms of SiO_2, CaO, MgO, Al_2O_3, Na_2O, K_2O, and H_2S (corresponding to the "SO_3" content of the slag in Table 4) only, except for a variable oxide component (Al_2O_3, MgO or CaO), which was specified according to the simulation conducted. A simulated slag reaction extent of 60% was employed, which represents a typical degree of reaction quantified for GBFS in sodium silicate-activated slag cements (~48% at 180 days in (Ben Haha et al., 2011a), 54 ±3% at 100 days in (Le Saoût et al., 2011), 58-61% at 180 days in (Bernal et al., 2014b) and >70% after 1 month in (Myers et al., 2015a)). A density of 2.8 g/cm^3 was selected for the unreacted slag component (Bernal et al., 2015).

Specific details pertaining to the descriptions of the slags simulated here, for each other aspect of the study, are shown near the beginning of each of sections 3.2-3.4.

3. Results and discussion

3.1 Utility of the CNASH_ss and MA-OH-LDH_ss thermodynamic models

Figure 2A shows that the calculated phase assemblage in NS-activated slag (NS-AS) cement changes as a function of Al_2O_3 content in the slag. The phase assemblage is dominated by C-(N-)A-S-H gel, in addition to MA-OH-LDH at all Al_2O_3 contents, and strätlingite, which also forms between 9 and 20 mass% Al_2O_3. Mg-Al LDH phases are commonly identified in sodium silicate-activated slag cements derived from slags with ≥5 mass% MgO (Bernal et al., 2014b), in good agreement with these results; LDH formation is reassessed in detail below. The simulated volume of the MA-OH-LDH phase does not change greatly here because its formation is limited by the amount of Mg supplied by the slag, which is constant at a fixed slag reaction extent. Small amounts of katoite are predicted for slags with 7-11 mass% Al_2O_3, which is relatively consistent with the observation of small amounts of this phase in sodium silicate-activated slag cements produced from slags with ~13 mass% Al_2O_3 (Bernal et al., 2014b; Schneider et al., 2001). Natrolite is predicted between 17 and 20 mass% slag Al_2O_3 content and very small quantities of brucite are predicted for slags with <7 mass% Al_2O_3.

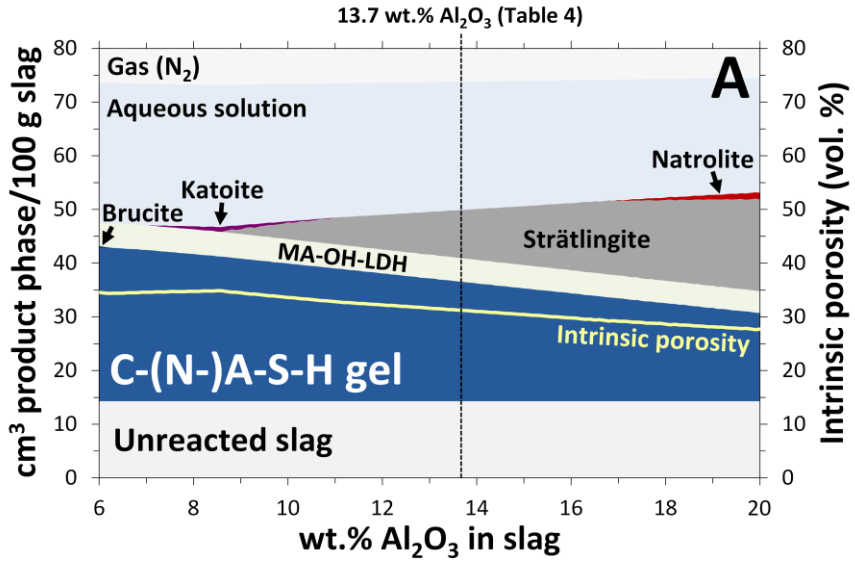

306

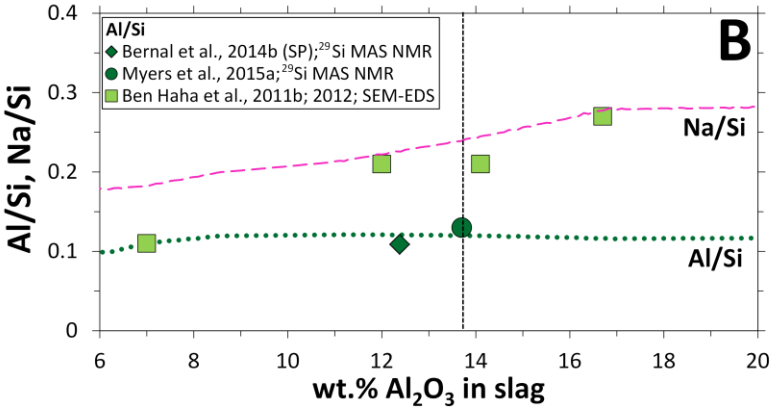

307

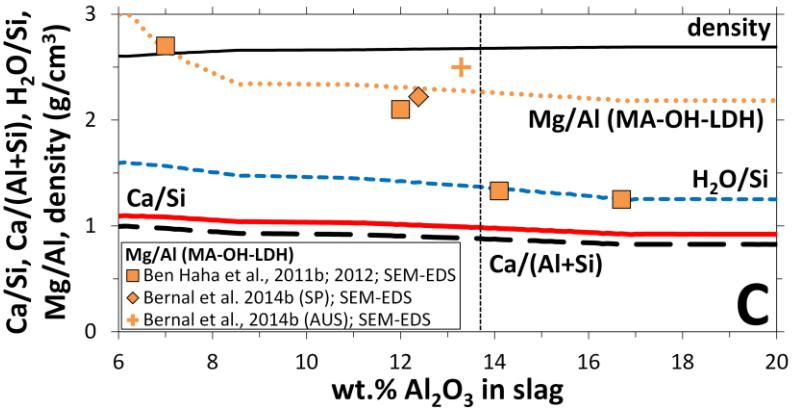

308

309 Figure 2. Simulated A) solid phase assemblages, B) Al/Si ratios in C-(N-)A-S-H gel, and C) Mg/Al
310 ratios in MA-OH-LDH in NS-AS cements with bulk slag chemical compositions rescaled from Table
311 4 except for the Al_2O_3 content, which is varied here. Changes in B) Na/Si, C) H_2O/Si, Ca/Si and
312 Ca/(Al+Si) ratios in C-(N-)A-S-H gel, and C) C-(N-)A-S-H gel density (g/cm^3) are shown for visual
313 reference. The symbols in B) and C) are experimental results for sodium silicate-activated slag
314 cements cured for 180 days and derived from slag precursors with similar MgO and equivalent or
315 slightly lower CaO content (5.2 < mass% MgO < 7.7, 35 < mass% CaO ≤ 42.6) to the slag
316 represented by Table 4.
317

318 The Mg/Al ratio of the simulated MA-OH-LDH phase is between 2 and 3 over the full range of
319 simulated slag Al_2O_3 compositions (Figure 2C), in excellent agreement with experimentally
320 determined Mg/Al ratios for this phase by scanning electron microscopy (SEM) with energy-
321 dispersive X-ray spectroscopy (EDS) analysis in sodium silicate-activated slag cements for slags
322 containing $7 \leq$ mass% $Al_2O_3 \leq 13.3$ (Ben Haha et al., 2012; Bernal et al., 2014b). However, the
323 experimental SEM-EDS data suggest a systematic reduction in the Mg/Al ratio of this phase to below
324 2 as a function of increasing slag Al_2O_3 content (Ben Haha et al., 2012; Bernal et al., 2014b), that was
325 not captured by the modelling performed here, as the MA-OH-LDH_ss thermodynamic model only
326 describes solid solutions in the range $2 \leq Mg/Al \leq 4$. Regions with Mg/Al ratios < 2 identified in
327 transmission electron microscopy (TEM)-EDS analysis of hydrated PC/GBFS cements (Taylor et al.,
328 2010) are discussed in terms of intimate mixtures of Mg-Al LDH and $Al(OH)_3$-type phases because
329 the chemical composition of Mg-Al LDH is theoretically limited to the range modelled here, $2 \leq$
330 $Mg/Al \leq 4$ (Richardson, 2013). The experimental Mg/Al ratios < 2 shown in Figure 2C can thus be
331 described similarly, which would explain the difference between the modelled and experimentally
332 measured data. This analysis suggests a need for additional thermodynamic data describing Al-rich
333 and Mg-poor solid phases that are not currently included in the thermodynamic database (e.g. TAH
334 (Andersen et al., 2006)) rather than a deficiency in the MA-OH-LDH_ss thermodynamic model as
335 such.
336
337 The amount of C-(N-)A-S-H gel formed in the simulated NS-AS cements decreases with increasing
338 Al_2O_3 content of the slag (Figure 2A) at the expense of strätlingite precipitation. An Al/Si ratio ≈ 0.12
339 is calculated for C-(N-)A-S-H gel in NS-AS cements derived from slags with >8 mass% Al_2O_3
340 (Figure 2B), which corresponds closely to the Al/Si ratios determined for this phase by analysis of
341 deconvoluted ^{29}Si magic angle spinning nuclear magnetic resonance (MAS NMR) spectra for these
342 materials at 180 days of age (Bernal et al., 2014b; Myers et al., 2015a) using the CSTM (Myers et al.,
343 2013). The CSTM is a structural model that represents C-(N-)A-S-H gel in terms of mixed cross-
344 linked/non-cross-linked components that enables chemical compositions and structural parameters to
345 be determined from deconvolution analysis of ^{29}Si MAS NMR spectra for materials containing this

346 phase. However, the experimental Al/Si ratios determined from ^{29}Si MAS NMR shown here exclude
347 the potential uptake of Al[5] (Andersen et al., 2006) and Al[6] (Sun et al., 2006) in C-(N-)A-S-H gel,
348 so are expected to be slightly lower than the 'true' Al/Si ratio in this phase. This discrepancy is
349 discussed further in section 3.2. However, the much higher Al/Si ratios shown by the other SEM-EDS
350 data, with Mg/Al < 2, could indicate mixtures of C-(N-)A-S-H gel with Mg-free and Al-containing
351 phases in the interaction volumes analysed by SEM-EDS. This description is similar to the analysis
352 above for Mg-Al LDH, so the thermodynamic modelling results are not necessarily inconsistent with
353 these experimental SEM-EDS data.
354
355 The total binder volume (solid + aqueous phases) is calculated to be approximately constant over the
356 full range of slag Al_2O_3 compositions studied (Figure 2A), suggesting that the bulk Al content of the
357 slag in NS-AS cements should not greatly affect the chemical shrinkage properties of these materials.
358 The results indicate a 20% change in intrinsic porosity (defined as the ratio of aqueous phase volume
359 to total binder volume, where water chemically bound in, or adsorbed to, the solid phases described in
360 Table 1 is considered to be a component of the solid) for slag compositions between ~8 and 20 mass%
361 Al_2O_3. This interpretation corresponds to the simulated C-(N-)A-S-H gel density of 2.5-2.7 g/cm^3 and
362 H_2O/Si ratios between 1.3 and 1.7 (in agreement with C-(N-)A-S-H gel at RH ≈ 25% (Muller et al.,
363 2013)), as shown in Figure 2C. Therefore, this phase is conceptually equivalent to C-(N-)A-S-H gel
364 with interlayer and some adsorbed water but no 'gel' or 'free' water (Jennings, 2008). However, the
365 reduced intrinsic porosity found here at higher bulk slag Al_2O_3 content does not explain the weak
366 dependency of sodium silicate-activated slag cement compressive strengths on bulk slag Al_2O_3
367 content (Ben Haha et al., 2012), because an increase in compressive strength would be expected at
368 lower porosity. This discrepancy is attributed to the higher amount of strätlingite simulated here
369 compared to the amount of this phase which is identified in AAS cements; this issue is revisited in
370 section 3.2.
371
372 Simulations of NS-AS cements derived from slags with 0-18 mass% MgO (Figure 3) show little
373 change in intrinsic porosity and total binder volume as a function of MgO content. This result differs

374 from previous thermodynamic modelling that showed a significant increase in total solid volume over
375 this same MgO composition range (Ben Haha et al., 2011b). This difference is partly founded in the
376 high amounts of strätlingite predicted, but also relates to the use of the CNASH_ss thermodynamic
377 model here, rather than the less complex thermodynamic model used to describe C-(N-)A-S-H gel by
378 Ben Haha et al. (2011b) (density ≈ 2.2-2.4 g/cm^3 (Lothenbach et al., 2008)), as the current work
379 formally defines the uptake of Al in C-(N-)A-S-H gel and much more closely describes the volumetric
380 properties of this phase in sodium silicate-activated slag cement (density = 2.6-2.7 g/cm^3 in Figure
381 3C, compared to 2.73 ± 0.02 g/cm^3 reported by Thomas et al. (2012)).
382
383

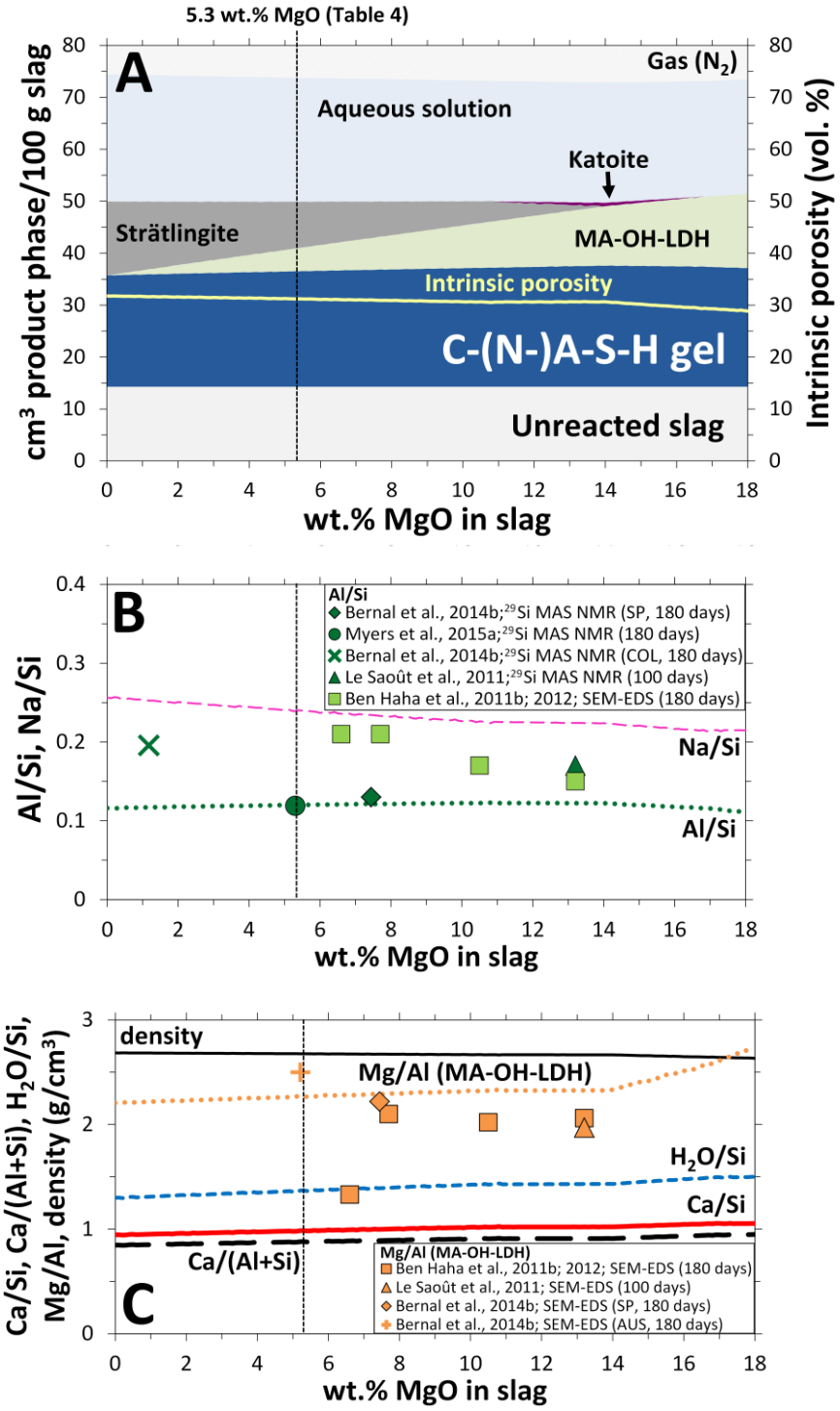

Figure 3. Simulated A) solid phase assemblages, B) Al/Si ratios in C-(N-)A-S-H gel, and C) Mg/Al ratios in MA-OH-LDH in NS-AS cements with bulk slag chemical compositions rescaled from Table 4 except for the Mg content, which is varied here. Changes in B) Na/Si, C) H_2O/Si, Ca/Si and Ca/(Al+Si) ratios in C-(N-)A-S-H gel, and C) C-(N-)A-S-H gel density (g/cm^3) are shown for visual reference. The symbols in B) and C) represent experimentally measured data for sodium silicate-activated slag cements (curing times are indicated in parentheses) derived from slag precursors with similar Al_2O_3 and equivalent or slightly lower CaO content (11.3 < mass% Al_2O_3 < 14.1, 33.4 < mass% CaO ≤ 42.6) to the slag represented by Table 4.

The solid phase assemblage changes markedly as a function of the MgO content of the slag (Figure 3A), but little change in C-(N-)A-S-H gel volume is simulated between 0 and 18 mass% MgO. The only Mg-bearing solid phase predicted is MA-OH-LDH, the amount of which increases as a function of the slag MgO content. The simulated and experimentally measured Mg/Al ratios of this phase in sodium silicate-activated slag cements are consistent to ±0.3 units (simulated Mg/Al ≈ 2.3, Figure 3C) (Ben Haha et al., 2011b; Bernal et al., 2014b; Le Saoût et al., 2011), with the exception of the samples containing significant intermixing of additional products (with Mg/Al << 2). This result further supports the thermodynamic description of MA-OH-LDH used here. The only predicted minor phase is katoite at 11-17 mass% MgO. Brucite is not predicted here, in good agreement with its absence from experimentally observed solid phase assemblages in AAS cements (Ben Haha et al., 2011b; Myers et al., 2015a; Richardson et al., 1994; Schneider et al., 2001; Wang and Scrivener, 1995).

The Al/Si ratio of the simulated C-(N-)A-S-H gel (Al/Si ≈ 0.12) is similar to the experimentally determined Al content of this phase in sodium silicate-activated slag cements derived from slags with 13.2 ≥ mass% MgO (Bernal et al., 2014b; Le Saoût et al., 2011) (Figure 3B), except for the SEM-EDS datum at ~7.8 mass% MgO (Ben Haha et al., 2012) and the ^{29}Si MAS NMR datum at 1.2 mass% MgO (Al/Si ≈ 0.2) (Bernal et al., 2014b). This discrepancy can be partly attributed to the incomplete description of solid phases in the thermodynamic database, which would be particularly relevant for the datum at 1.2 mass% MgO, as gismondine and/or N-A-S(-H) gel (which is thought to be a poorly-ordered zeolite-type phase (Provis et al., 2005)) were identified as reaction products in the cement studied by Bernal et al. (2014b). Simulations of NS-AS cements show that Ca-heulandite and natrolite are predicted for slags with ≤41 mass% CaO (Figure 4), in good agreement with this analysis and the identification of zeolites in these materials (Bernal et al., 2011; Bernal et al., 2014b). The bulk CaO concentration is therefore a key parameter controlling the formation of zeolite-type phases in AAS-based cements. However, it is important to note that Ca-rich zeolites such as gismondine, which are expected to have relatively high stability in AAS-based cements, are not described in the thermodynamic database used here because reliable thermodynamic data for these phases are not always available (Wolery et al., 2007).

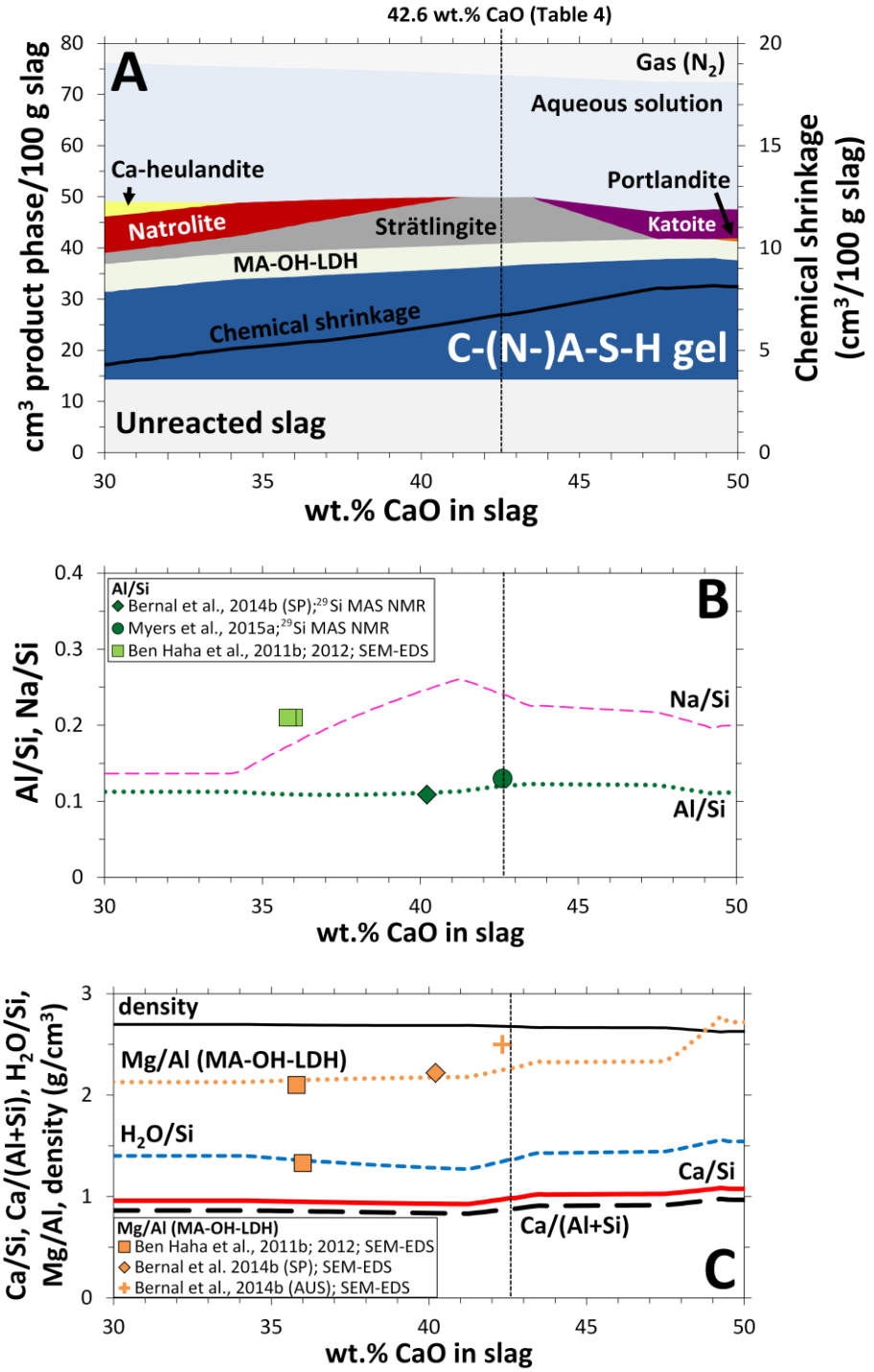

Figure 4. Simulated A) solid phase assemblages, B) Al/Si ratios in C-(N-)A-S-H gel, and C) Mg/Al ratios in MA-OH-LDH in NS-AS cements with bulk slag chemical compositions rescaled from Table 4 except for the Ca content, which is varied here (traces). Changes in B) Na/Si, C) H_2O/Si, Ca/Si and Ca/(Al+Si) ratios in C-(N-)A-S-H gel, and C) C-(N-)A-S-H gel density (g/cm^3) are shown for visual reference. The symbols in B) and C) represent experimentally measured data for sodium silicate-activated slag cements derived from slag precursors with similar Al_2O_3 and MgO content (12 < mass% Al_2O_3 < 14.1, 5.2 < mass% MgO < 7.7) to the slag represented by Table 4. The difference in intrinsic porosity within the full range of modelled CaO compositions is 3%.

436 It is also notable that the total binder (solid + aqueous phase) volume changes markedly as a function
437 of the CaO content in the slag, which suggests that the bulk CaO concentration is also a key parameter
438 influencing the chemical shrinkage properties of these materials; a difference of 3.8 cm^3/100 g slag
439 (Δchemical shrinkage = 47%) is identified over the range $30 \leq CaO \leq 49$ mass%, with more chemical
440 shrinkage predicted at higher slag CaO content (Figure 4A). Therefore, it is expected that chemical
441 shrinkage in NS-AS cements can be reduced through the use of raw materials with lower CaO
442 content. Simulated Mg/Al ratios of the MA-OH-LDH phase and Al/Si ratios of C-(N-)A-S-H gel are
443 in close agreement with the experimental data, with the exception of the SEM-EDS data at a slag CaO
444 content of ~36 mass% which likely contains some intermixed low-Mg high-Al phases (Taylor et al.,
445 2010).
446
447 The modelling results presented here provide a satisfactory account of the experimental data and so
448 give confidence in using the CNASH_ss and MgAl-OH_LDH_ss thermodynamic models to describe
449 NS-AS cements over the most common ranges of slag compositions and activator doses used in AAS
450 cements ($7 \leq$ mass% $Al_2O_3 \leq 13.7$, Figure 2, $5.2 \leq$ mass% $MgO \leq 13.2$, Figure 3, and $35.8 \leq$ mass%
451 $CaO \leq 42.3$, Figure 4). Within this range, the model predictions are within ~0.04 units in the Al/Si
452 ratios of the C-(N-)A-S-H gel and ~0.3 units in the Mg/Al ratios of the MA-OH-LDH phase.
453

454 3.2 Simulated reaction of a Na_2SiO_3-activated slag cement

455 Additional thermodynamic modelling analysis of NS-AS cements was performed by varying the slag
456 reaction extent from 0-100%, in the presence of Na_2SiO_3 (8 g Na_2SiO_3/100 g slag), while holding the
457 slag chemical composition constant (Table 4).
458
459 The predicted solid phase assemblage consists of C-(N-)A-S-H gel as the dominant reaction product,
460 and additionally MA-OH-LDH (Mg/Al ≈ 2), strätlingite, Ca-heulandite, brucite, natrolite and katoite
461 (Figure 5A). Zeolites are only predicted for slag reaction extents <40% (i.e. effectively at low bulk
462 CaO concentrations, consistent with Figure 4), which is less than the experimentally-determined slag

463 reaction extent for AAS cement after 1 day of curing (Myers et al., 2015a), and is relatively consistent
464 with the experimental observation of only minor amounts of these phases in AAS cements (Bernal et
465 al., 2011; Bernal et al., 2014b).
466
467 The prediction of MA-OH-LDH and strätlingite is in relatively good agreement with experimentally-
468 determined solid phase assemblages in NS-AS cements (Ben Haha et al., 2012; Brough and Atkinson,
469 2002; Burciaga-Díaz and Escalante-García, 2013; Myers et al., 2015a; Wang and Scrivener, 1995),
470 where Mg-Al LDH phases are often identified and the formation of AFm-type phases are likely,
471 although the calculations here do markedly over-predict the amount of strätlingite formed compared
472 to the experimental observations. Approximately constant proportions of the main hydrate phases
473 (strätlingite, MA-OH-LDH and C-(N-)A-S-H gel) are predicted relative to the total reaction product
474 volume at slag reaction extents exceeding 40%. The influence of the additional Si supplied by the
475 activator is diluted as more slag reacts, as the activator is assumed to be fully dissolved in the mix
476 water prior to contact with the slag, and so contributes more significantly to the chemistry of the
477 reaction products when the degree of reaction of the slag is low. This means that the slag chemical
478 composition, rather than the activator, controls the stable product phase assemblage at higher extents
479 of reaction.
480
481 The chemical shrinkage in this system is predicted to be 11 cm^3/100 g slag at complete reaction of the
482 slag (an overall volume reduction of 15%, Figure 5A), which matches the chemical shrinkage
483 quantified experimentally by Thomas et al. (2012) for a sodium silicate-activated slag cement (12.2 ±
484 1.5 cm^3/100 g slag) and is close to the values modelled by Chen and Brouwers (2007) (11.5-13.9
485 cm^3/100 g slag) at 100% degree of reaction of the slag. Therefore, thermodynamic modelling predicts
486 significantly larger chemical shrinkage in NS-AS cements than measured in hydrated PC (~6 cm^3/100
487 g cement reacted (Jensen and Hansen, 2001; Tazawa et al., 1995)).
488

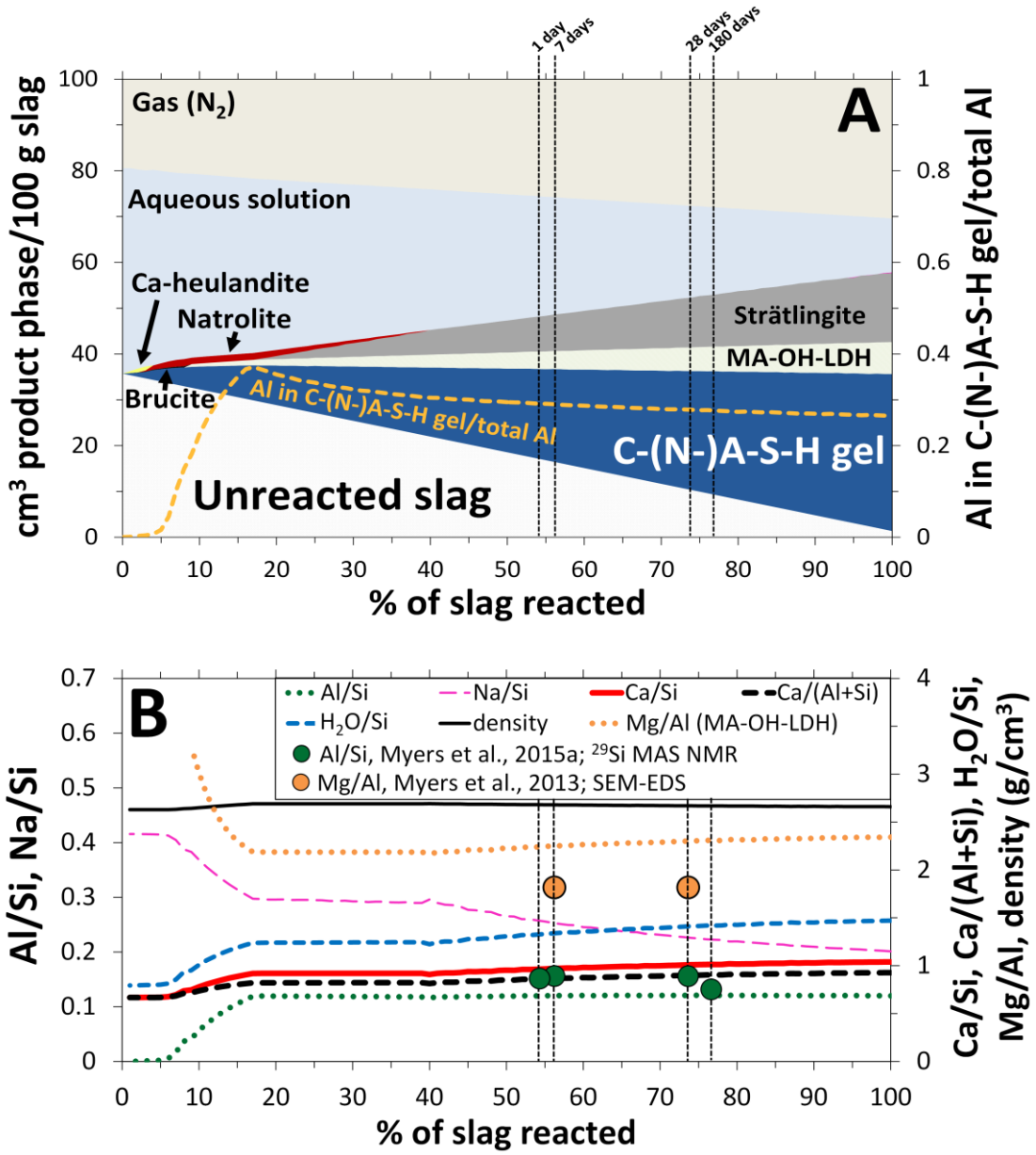

Figure 5. Simulated A) solid phase assemblages, and B) Al/Si ratios in C-(N-)A-S-H gel and Mg/Al ratios in MA-OH-LDH in an NS-AS cement using the slag chemical composition in Table 4. Changes in B) Na/Si, H_2O/Si, Ca/Si and Ca/(Al+Si) ratios in C-(N-)A-S-H gel, and B) C-(N-)A-S-H gel density (g/cm^3) are shown for visual reference. The dashed vertical lines correspond to slag reaction extents determined experimentally at each time of curing (Myers et al., 2015a).

The increased Ca content and decreased Na/Si ratio of the C-(N-)A-S-H gel at higher slag reaction extents (Figure 5B) are reflected in the reduced bulk Si and Na concentrations and the relative decrease in the fraction of Na-containing end-members simulated as the alkali activation reaction progresses (Figure 6). A ~50% reduction in the concentration of Na in the pore solution is predicted from 0 to 100% slag reaction extent, although a constant pH of ~14 is maintained and >10 times more Na is always predicted to be present in the aqueous phase relative to C-(N-)A-S-H gel. The simulated

amounts of H_2O and Ca in C-(N-)A-S-H gel are directly linked via the end-member chemical compositions defined in the CNASH_ss thermodynamic model (Myers et al., 2014): the Ca-rich T2C* end-member (Ca/Si = 1.5) has a higher H_2O/Si ratio (= 2.5) compared to the Al and Na-containing end-members (H_2O/Si < 2, Table 1), and relatively more of this end-member is simulated at higher bulk slag reaction extents (Figure 6B). The simulated trends in pore solution element concentrations at >40% slag reaction extent (Figure 6A) are within ±1 order of magnitude to those reported for NS-AS cement cured for 1-180 days (Gruskovnjak et al., 2006). More solubility data for NS-AS cement are needed to further assess the simulated pore solution compositions.

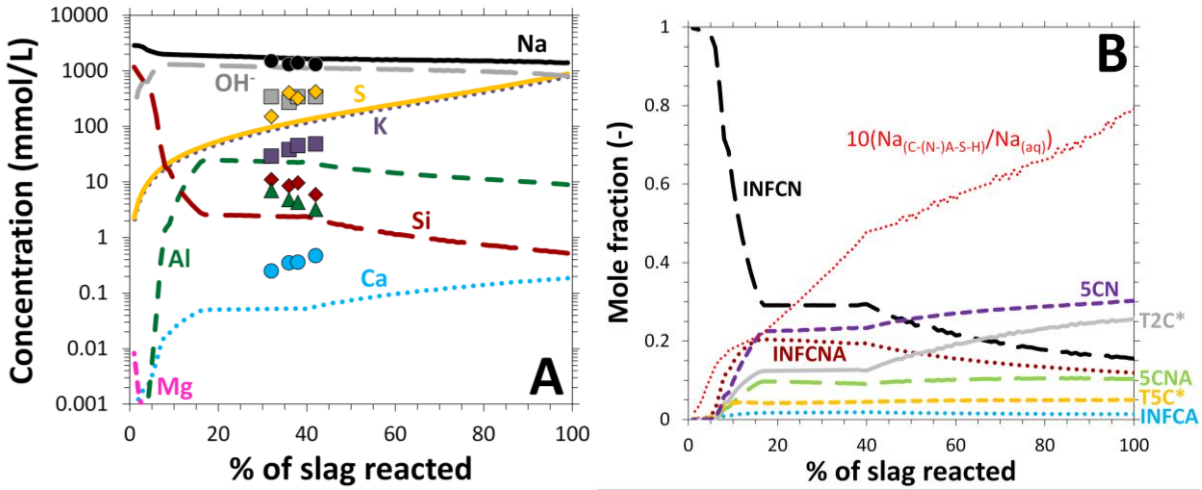

Figure 6. Simulated A) pore solution chemical compositions and B) end-member mole fractions and ratio of Na in C-(N-)A-S-H gel relative to Na in the aqueous phase (aq) for the NS-AS cement described by Figure 5. The mole fraction of the TobH* end-member is close to 0 over the full range of simulated slag reaction extents (not shown in B)). The symbols in A) represent sodium silicate-activated slag pore solution data reported by Gruskovnjak et al. (2006).

The simulated fraction of Al in MA-OH-LDH relative to the total amount of Al in the reaction products ($Al_{MgAl\ LDH}/Al_{products}$) is ~0.22, which is consistent with deconvolution analysis of ^{27}Al MAS NMR spectra for the analogous experimental NS-AS cement between 1-180 days of curing ($Al_{MgAl\ LDH}/Al_{products}$ = 0.18-0.26) (Myers et al., 2015a), but the predicted Mg/Al ratios are greater than those measured by SEM-EDS analysis for this material (Figure 5B). This result provides further support for explaining Mg/Al ratios < 2 in terms of intimately intermixed low-Mg high-Al phases with Mg-Al LDH phases, e.g. TAH or N-A-S(-H) gel, because the low Mg/Al ratio of this solid solution phase is 2

526 (Richardson, 2013). However, the simulations predict that the fraction of Al in C-(N-)A-S-H gel
527 (Al_{CNASH}) relative to the total amount of Al in the reaction products ($Al_{CNASH}/Al_{products}$) is ~0.28 for
528 slag reaction extents >50% (Figure 5A), which is much less than the relative amount of four-
529 coordinated Al (Al[4]) assigned to the reaction products ($Al[4]/Al_{products}$) in ^{27}Al MAS NMR spectral
530 deconvolution analysis of this NS-AS cement ($Al[4]/Al_{products}$ = 0.60-0.75) (Myers et al., 2015a).
531 These ratios, $Al_{CNASH}/Al_{products}$ and $Al[4]/Al_{products}$, would be comparable if C-(N-)A-S-H gel were the
532 only major Al[4]-bearing solid phase present in AAS cements (i.e. $Al_{CNASH}/Al[4] \approx 1$), but that is not
533 the case here. Recent solubility results for C-(N-)A-S-H gel (Myers et al., 2015b) do not support any
534 further increase in the stability of the Al-containing end-members in the CNASH_ss thermodynamic
535 model, meaning that this discrepancy in the distribution of Al[4] is probably due to other factors.
536 These factors may include incomplete description of other Al[4]-containing phases in the
537 thermodynamic database used here, or that the discrepancy is founded in the experimental ^{29}Si and
538 ^{27}Al MAS NMR analysis. Both options are now discussed.
539
540 The amount of strätlingite predicted by the thermodynamic modelling (Figures 2-5) was likely
541 overestimated because this phase is not clearly distinguished in X-ray diffractograms of sodium
542 silicate-activated slag cements cured for up to 3 years (Ben Haha et al., 2012; Burciaga-Díaz and
543 Escalante-García, 2013; Wang and Scrivener, 1995), or in NS-AS/4 mass% PC blends cured for 3
544 years (Bernal et al., 2012). The solubility product used to describe this phase (Table 1) has an
545 estimated uncertainty interval of ±1 log unit derived directly from the scatter in the available
546 solubility data for this phase (see Matschei et al. (2007) and references therein), and so an error in this
547 value is unlikely to contribute significantly to the over-prediction of this phase. Therefore, it is likely
548 that additional solid phase(s) are missing from the thermodynamic database used here (Table 1),
549 which would be predicted to form in preference to strätlingite if they were present in the simulation.
550 These may be zeolites such as gismondine and thomsonite (Bernal et al., 2011; Bernal et al., 2014b),
551 or poorly ordered Q^4-type N-A-S(-H) ('geopolymer') gels (Myers et al., 2013), each of which will
552 accommodate Al in tetrahedral form and could account for the difference between the high tetrahedral
553 fraction determined experimentally, and the notably lower tetrahedral fraction predicted in the current

simulations. Thermodynamic data are available for a large number of zeolites (see the compilation by Arthur et al. (2011) for example), but the large variety of possible chemical compositions and the availability of only a few data for each zeolite framework type (often only one datum), mean that more thermochemical or solubility data are needed to better define these phases in thermodynamic databases.

The maximum possible amount of Al[4] attributable to zeolites or N-A-S(-H) gel is, however, limited by the intensity of the ^{27}Al MAS NMR spectra of this NS-AS cement (Myers et al., 2015a) at ~60 ppm (relative to $Al(H_2O)_6^{3+}$), which is the typical observed chemical shift at which Al[4] resonates in these phases (Davidovits, 1991; Duxson et al., 2007; Fyfe et al., 1982). Consequently, it is unlikely that zeolites and N-A-S(-H) gel can account for the large discrepancy between the modelled amount of Al[4] in C-(N-)A-S-H gel ($Al_{CNASH}/Al_{products} \approx 0.28$, Figure 5A) and the experimentally observed amount of Al[4] assigned to reaction products ($Al[4]/Al_{products}$ = 0.60-0.75 (Myers et al., 2015a)). Further explanation for this discrepancy can be found in the assumption of congruent slag dissolution applied in the analysis of ^{29}Si and ^{27}Al MAS NMR spectra used as experimental data here (Bernal et al., 2014b; Myers et al., 2015a), which may not be fully attained in slag-based cements, and could significantly alter the deconvolution analysis presented due to the different lineshapes of partially reacted and unreacted slag (Dyson et al., 2007). Development of this understanding will be essential to further enhance the accuracy of the characterisation and simulation of the complex phase assemblages which are formed in AAS-based cements.

3.3 Simulated reaction of a Na_2CO_3-activated slag cement

The reaction of a N<u>c</u>-AS cement is simulated via the same procedure used in the simulation of NS-AS cement discussed in section 3.2, except for the change in activator. The simulated solid phase assemblage contains C-(N-)A-S-H gel as the primary reaction product (Figure 7A). The additional products are $C_4A\underline{c}H_{11}$, MA-OH-LDH, calcite and natrolite. The prediction of calcite is consistent with the observation of $CaCO_3$ polymorphs in N<u>c</u>-AS cements cured for 20 months (Sakulich et al., 2010)

and 180 days (Bernal et al., 2015). Simulation of natrolite and Ca-heulandite is also in good agreement with the identification of heulandite and zeolite-A in Nc-AS cement (Bernal et al., 2015). The modelling results presented here and in section 3.3 are consistent with the identification of more prominent peaks for zeolites in X-ray diffraction patterns for Nc-activated (Bernal et al., 2015), compared to NS-activated, slag cements (Bernal et al., 2014b). C_4AcH_{11} has been identified in X-ray diffractograms of Nc-AS pastes cured for 1 day and for 540 days (Shi et al., 2006), although this phase is not always observable (Bernal et al., 2015; Sakulich et al., 2010) due to its tendency to be present as intermixed (Richardson et al., 1994) and/or poorly crystalline structures (Wang and Scrivener, 1995). The simulated chemical shrinkage extents for Nc-AS (Figure 7) and NS-AS cements (Figure 5) at 100% slag reaction extent are comparable, at 11 cm^3/100 g slag.

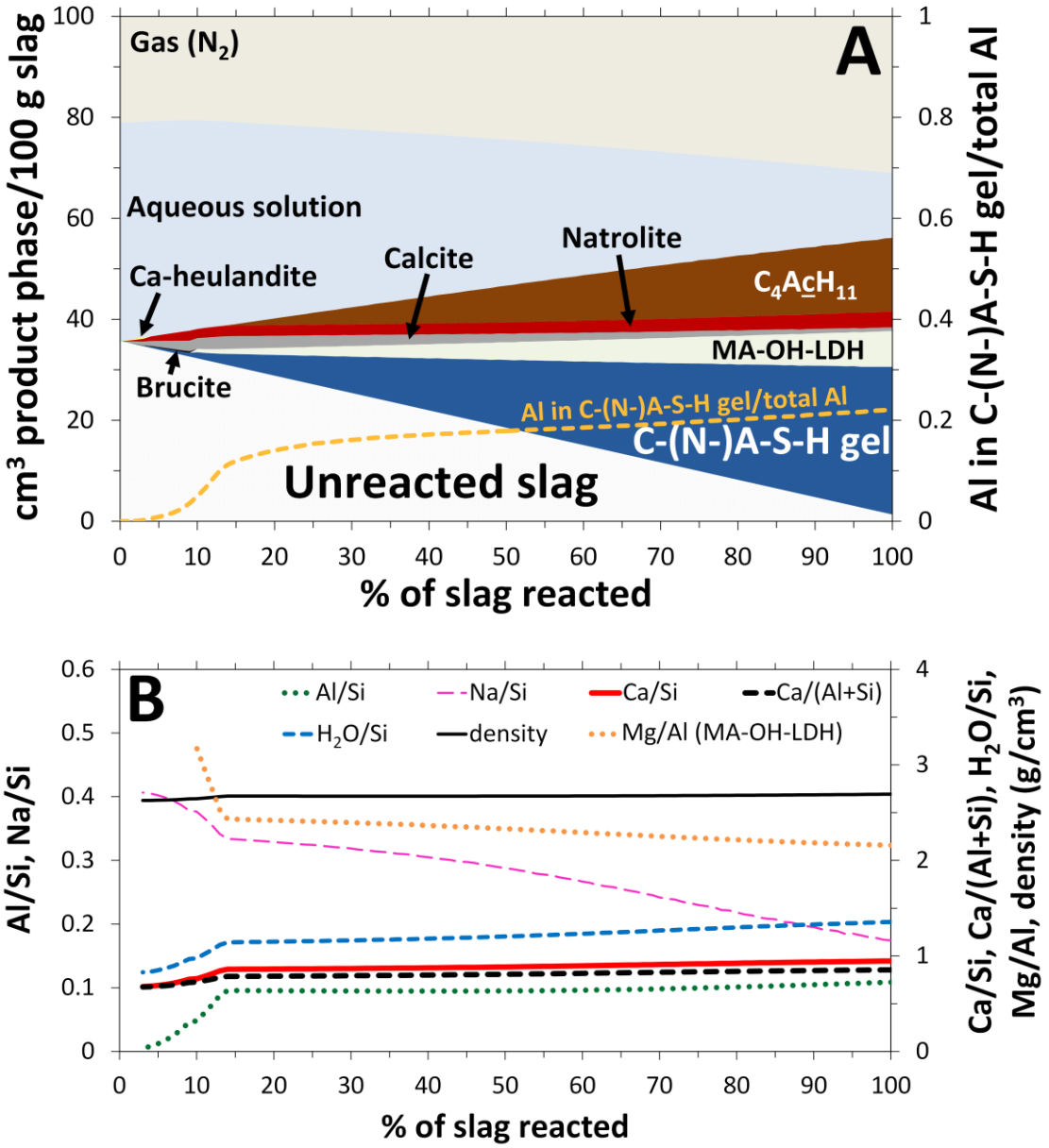

Figure 7. Simulated A) solid phase assemblages and B) C-(N-)A-S-H gel chemical compositions and densities (g/cm^3), and Mg/Al ratios in MA-OH-LDH in an Nc-AS cement using the slag chemical composition in Table 4.

Mg-Al LDH phases are experimentally observed in Nc-AS cements after 180 days (Bernal et al., 2015) and 55 days (Sakulich et al., 2009) of curing, in good agreement with the predicted phase assemblage (Figure 7A). Here, MA-c-LDH is not predicted despite the high availability of CO_2, demonstrating the very high stability of MA-OH-LDH under the pH $\geq$ 13 conditions in a hardened Nc-AS cement. Further clarification of this result is needed because recent ^{27}Al MAS NMR results for superficially carbonated NS-AS cements (Myers et al., 2015a), and carbonation depth analysis of

these materials after exposure to air for 16 months (Bernal et al., 2014b) can be interpreted in support of the formation of Mg-Al LDH phases intercalated with CO_3^{2-}. Detailed assessment of solubility and thermochemical data for Mg-Al LDH phases intercalated with OH^- and CO_3^{2-} (Bennett et al., 1992; Gao and Li, 2012; Johnson and Glasser, 2003; Morimoto et al., 2012; Rozov et al., 2011) indicates that the solubility product used to describe the Mg/Al = 2 MA-OH-LDH end-member of the MA-OH-LDH_ss thermodynamic model here may be in error by as much as several log units (Figure 1) and demonstrates the need for further studies of the thermodynamic properties of Mg-Al LDH phases.

Gaylussite has been observed in Nc-AS cement at early age (Bernal et al., 2015) but is not present in the solid phase assemblage simulated here (Figure 7); this phase is slightly undersaturated at low slag reaction extents at ~25°C (Bury and Redd, 1933; Königsberger et al., 1999). This difference indicates that kinetic factors enable the formation of gaylussite in Nc-AS cement cured at room temperature, and this is consistent with its observed consumption as the reaction proceeds (Bernal et al., 2015).

3.4 Phase diagrams for alkali-activated slag-based cements

The prediction of several reaction products in the simulated AAS cements is consistent with the bulk chemical composition of the mixes, which generally lie outside the composition envelope of phase-pure C-(N-)A-S-H gel (Figure 8).

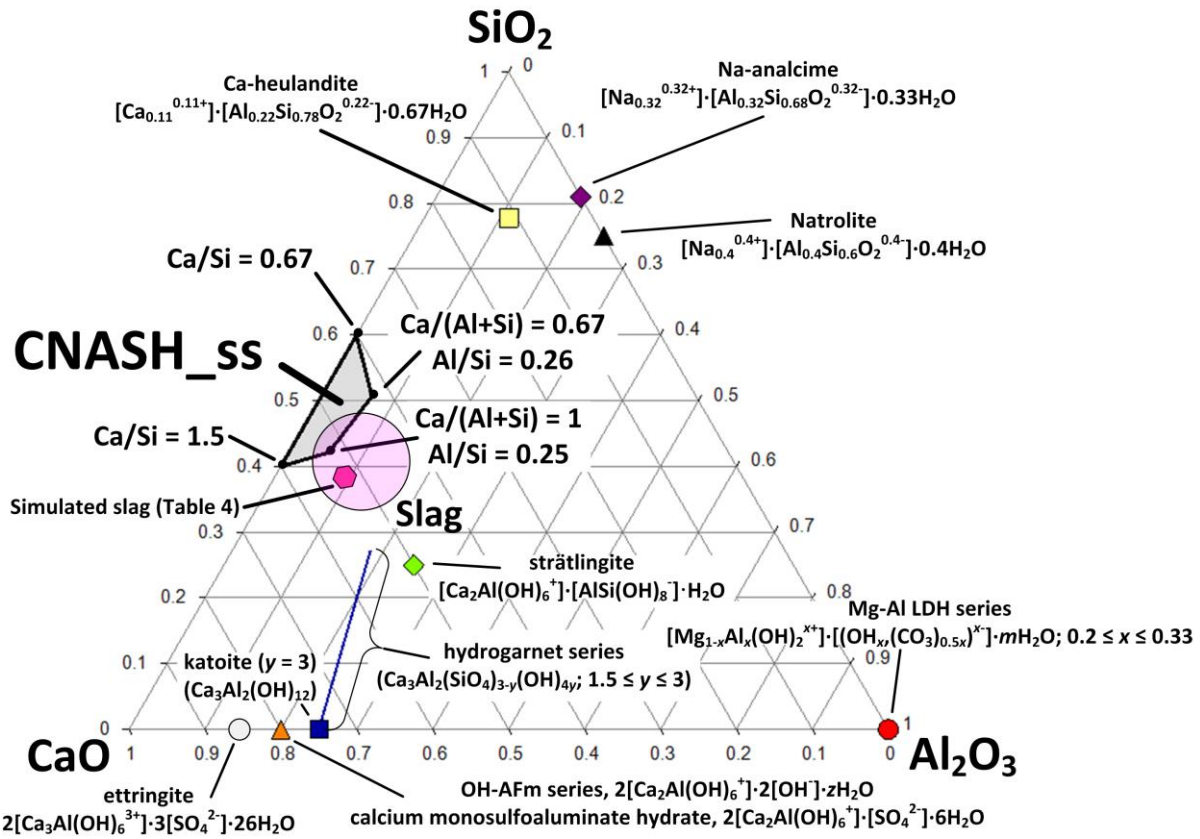

Figure 8. Projection of the chemical composition of some reaction products in AAS-based cements onto the CaO-SiO_2-Al_2O_3 ternary system. The grey and pink shaded regions are the composition range described by the CNASH_ss thermodynamic model for C-(N-)A-S-H gel (Myers et al., 2014), and the typical bulk chemical composition range of slag, respectively. The simulated slag described in Table 4 is represented by the pink hexagon.

Further analysis of AAS cement chemistry is performed by simulating phase diagrams at a fixed slag reaction extent of 60%, a constant amount of H_2S (equivalent in S content to a slag composition of 2 mass% SO_3, which is taken as a representative value of S content in slags studied in the literature (Ben Haha et al., 2011a; Bernal et al., 2014b; Gruskovnjak et al., 2006; Puertas et al., 2011; Richardson et al., 1994; Shi et al., 2006)) and slag compositions of either 30 or 40 mass% SiO_2, with the remaining chemical composition specified in terms of CaO, Al_2O_3 and MgO only. The CaO-Al_2O_3-MgO composition range selected here was chosen to represent the bulk chemical composition range relevant to AAS-based cements.

Zeolites are predicted in every phase diagram for the AAS cements simulated (shown for NS-AS cements only in Figure 9), and are more prominent at higher Si (i.e. lower Ca) and Al concentrations, but only Ca-heulandite and natrolite are predicted among the zeolites included in the thermodynamic

642 database (Table 1). The CaO-Al_2O_3-MgO composition region where C-(N-)A-S-H gel and zeolites are
643 both simulated indicates where C-(N-)A-S-H and N-A-S(-H) gels are likely to coexist in AAS
644 cements, due to the fundamental similarities of zeolites and N-A-S(-H) ('geopolymer') gels (Provis et
645 al., 2005). Inclusion of reliable thermodynamic data for N-A-S(-H) gel and zeolites will be necessary
646 to clarify the chemical compositional envelope in which these gels can coexist. The prediction of
647 zeolites here, in both the higher pH ($(NH)_{0.5}$-AS) and lower pH systems (Nc-AS), Figures 7 and 9,
648 indicates that increasing pH does not destabilise these phases and the corresponding N-A-S(-H) gel in
649 favour of C-(N-)A-S-H gel in the pH and chemical composition range relevant to cements, as was
650 proposed previously by García-Lodeiro et al. (2011). The increased stability of zeolites at lower CaO
651 content (Figure 4), or alternatively higher Si and Al concentrations (Figure 9) – i.e. decreasing
652 $CaO/(Al_2O_3 + SiO_2)$ – demonstrates that control of Ca-Al-Si compositions is needed to form alkali-
653 activated cements with mixed C-(N-)A-S-H and N-A-S(-H) gels (Ismail et al., 2014). Figure 9 shows
654 that mixtures of C-(N-)A-S-H gel and zeolites are expected to be stable in Na_2SiO_3-activated 75
655 mass% GBFS/25 mass% fly ash (FA) (overall precursor SiO_2 content = 41 mass% based on the FA
656 chemical composition from (Bernal et al., 2013)) or metakaolin (MK) cements (overall precursor SiO_2
657 content = 38 mass% based on the MK chemical composition from (Bernal et al., 2011)), but not in a
658 hybrid system of Na_2SiO_3-activated 75 mass% GBFS/25 mass% PC (based on a PC chemical
659 composition of 19.7 mass% SiO_2, 63.2 mass% CaO, 1.85 mass% MgO, 4.7 mass% Al_2O_3, 3.35
660 mass% SO_3 (Lothenbach and Winnefeld, 2006)). Figure 9 also shows that the stability of zeolites, and
661 therefore of N-A-S(-H) gels, in NS-AS cement depends greatly on the slag SiO_2 content.
662
663

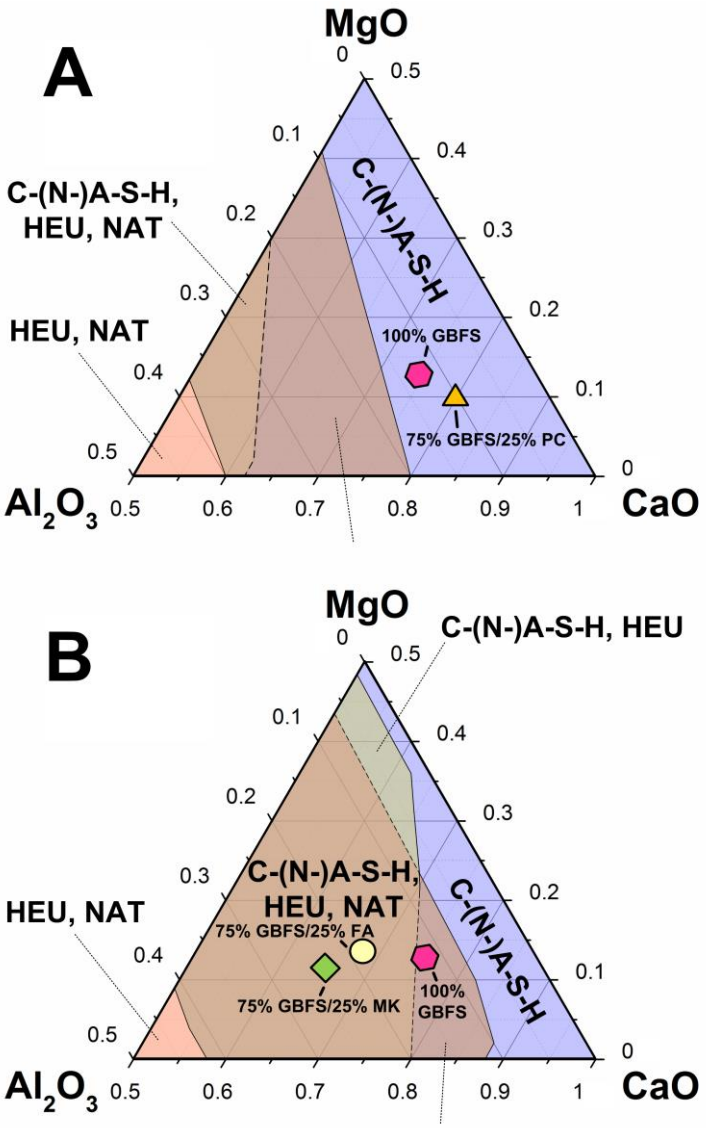

Figure 9. Phase diagrams for NS-AS-based cement systems with overall precursor chemical compositions of 2 mass% SO_3 equivalent and A) 30 mass% SiO_2 and B) 40 mass% SiO_2, with only the regions of stability for C-(N-)A-S-H gel and zeolites shown (Mg-containing phases are also typical reaction products: MA-OH-LDH at moderate and high Al_2O_3 content ($Al_2O_3/(CaO+Al_2O_3+MgO) > 0.1$); and brucite at moderate and low Al_2O_3 concentrations ($Al_2O_3/(CaO+Al_2O_3+MgO) < 0.25$)). See text for the GBFS, FA, MK and PC chemical compositions used. The w/b ratio is 0.4, the overall precursor reaction extent is 60% and the units are in mole fraction.

Simulated phase diagrams for $(NH)_{0.5}$-AS-based cements are shown in Figure 10. The dominant solids in the simulated phase diagrams for $(NH)_{0.5}$-AS-based cements (Figure 10) are C-(N-)A-S-H gel and MA-OH-LDH. C-(N-)A-S-H gel is simulated over the full range of modelled CaO-Al_2O_3-MgO compositions, and MA-OH-LDH is predicted everywhere in this composition range except at very low Al_2O_3 content ($Al_2O_3/(CaO+Al_2O_3+MgO) < 0.05$).

Symbol	Phase assemblage
a	1, 9, 10
b	1, 5, 9, 10
c	1, 5, 6, 9, 10
d	1, 2, 5, 6, 9, 10
e	1, 2, 4, 5, 6, 9, 10
f	1, 2, 5, 6, 10
g	1, 2, 5, 6
h	1, 2, 4, 5, 6
i	1, 2, 4, 5, 6, 10
j	1, 2, 3, 4, 5, 6, 10
k	1, 2, 3, 4, 5, 6
l	1, 2, 3, 5, 6
m	1, 2, 3, 5, 6, 7
n	1, 2, 5, 9, 10
o	1, 5, 6, 10
p	1, 5, 10
q	1, 2, 5, 6, 8, 10
r	1, 2, 5, 8, 10
s	1, 2, 5, 8
t	1, 2, 3, 5, 8
u	1, 2, 3, 5, 8, 10
v	1, 2, 3, 5, 7, 8, 10
w	1, 2, 3, 5, 7, 8
x	1, 2, 9, 10
y	1, 2, 5, 10

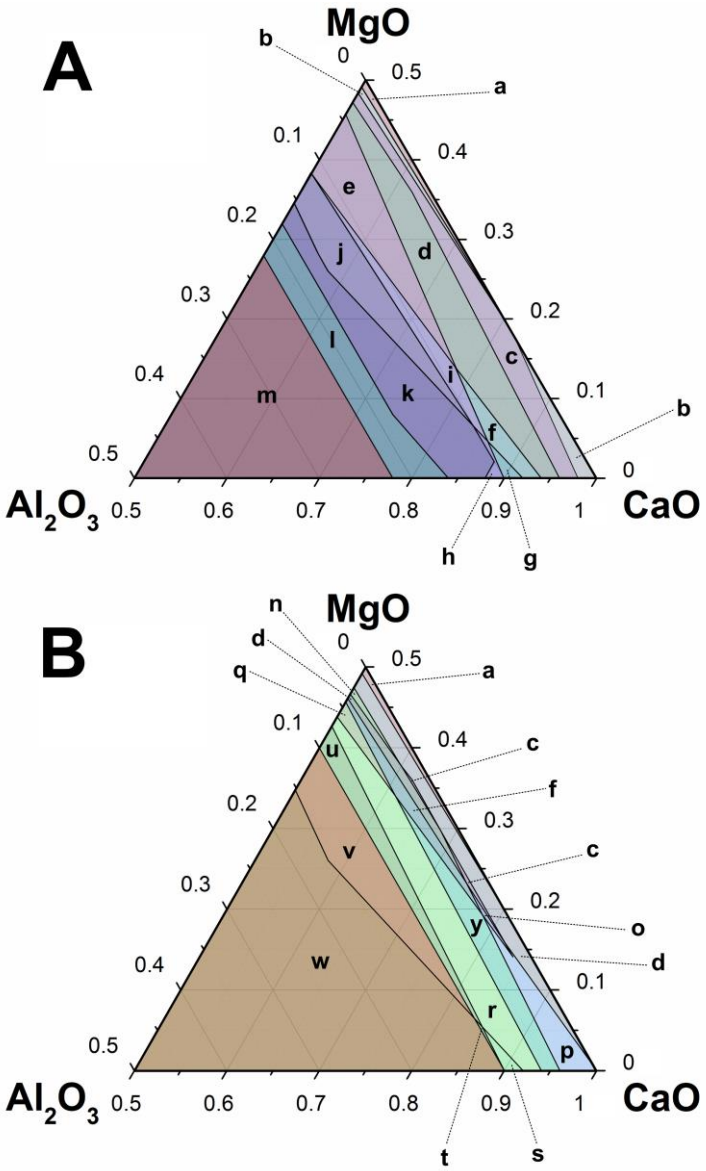

Figure 10. Phase diagrams in the relevant bulk CaO-Al_2O_3-MgO composition range for $(NH)_{0.5}$-AS-based cements with A) 30 and B) 40 mass% slag SiO_2 content, and 2 mass% SO_3 equivalent. The phases are: 1, C-(N-)A-S-H gel; 2, MA-OH-LDH; 3, strätlingite; 4, katoite; 5, ettringite; 6, calcium monosulfoaluminate hydrate; 7, natrolite; 8, Ca-heulandite; 9, portlandite; and 10, brucite. The w/b ratio is 0.4, the slag reaction extent is 60% and the units are in mole fraction.

Ettringite is predicted over a much larger range of CaO-Al_2O_3-MgO compositions than calcium monosulfoaluminate hydrate. These phases are predicted to form here for slag with 2 mass% SO_3 equivalent but not for slag containing 0.8 mass% equivalent SO_3 (Table 4). Katoite is only present in the phase diagrams for slags with 30 mass% SiO_2 in the $(NH)_{0.5}$-AS system. Portlandite is more prominent in the 30 mass% SiO_2 $(NH)_{0.5}$-AS system (Figure 10A), but is only formed at relatively low

Al_2O_3 content (Al_2O_3/(CaO+Al_2O_3+MgO) ≤ 0.12). Brucite is predicted in both phase diagrams, but not at high Al_2O_3 concentrations (Al_2O_3/(CaO+Al_2O_3+MgO) > 0.2). Natrolite and Ca-heulandite are the only zeolites simulated in the phase diagrams. Ca-heulandite has a larger stability region than natrolite in the 40 mass% SiO_2 system, but is not predicted at a SiO_2 content of 30 mass%, where only natrolite is simulated. However, the overall CaO-Al_2O_3-MgO composition region where zeolites are stable in $(NH)_{0.5}$-AS-based cements increases as a function of increasing slag SiO_2 content, which is consistent with the trends in zeolite stability described above for NS-AS-based cements (Figures 4 and 9). Similarly, the CaO-Al_2O_3-MgO composition range where strätlingite is stable is larger in the 40 mass% SiO_2 $(NH)_{0.5}$-AS cement system. These phases, strätlingite, natrolite and Ca-heulandite are only simulated for Al_2O_3/(CaO+Al_2O_3+MgO) ratios > 0.1, showing that intermediate to high Al concentrations are needed to stabilise these phases in $(NH)_{0.5}$-AS-based cements.

The phase diagrams presented here provide a framework for predicting solid phase assemblages in AAS cements, which can be improved with more relevant data, e.g. development of the thermodynamic database used (Tables 1-3). This work improves the way in which high-performance AAS-based cements can be designed, by linking the volumetric properties and solid phases formed in these cements to the raw materials used in their production. This framework also represents an important step towards predicting the durability of AAS-based cements, although further work is needed to link the key degradation mechanisms, e.g. carbonation, with the volumetric properties (Provis et al., 2012) and phase assemblages (Bernal et al., 2014b) in these cements.

4. Conclusions

This paper has presented a thermodynamic modelling analysis of AAS-based cements. The thermodynamic database used contains a CNASH_ss thermodynamic model for C-(N-)A-S-H gel, which explicitly describes Na and tetrahedral Al incorporated into this phase, a MA-OH-LDH_ss

ideal solid solution thermodynamic model for MA-OH-LDH, and thermodynamic data for some alkali carbonate and zeolite phases. The thermodynamic database presented here extends the utility of thermodynamic modelling in predicting the long-term chemistry of AAS-based cements, which is important for application of these materials, e.g. in the design of high performance cements for construction and in nuclear waste disposal applications, and further promotes the valorisation of metallurgical slags.

Thermodynamic modelling of NS-AS cements generally showed that the CNASH_ss thermodynamic model described the Al/Si ratios of the C-(N-)A-S-H gels formed in the most relevant composition range/alkali content for the majority of AAS cements. The Mg/Al ratios of the simulated MA-OH-LDH phase was generally in good agreement with experimental results for this phase in AAS cements, although additional thermodynamic data for MA-OH-LDH are needed to clarify the stability of this phase in carbonated and Nc-activated cement. Additional thermodynamic data for other reaction products such as TAH, zeolites and N-A-S(-H) gels are also needed for better consistency with the experimental Al/Si ratios in C-(N-)A-S-H gel and Mg/Al ratios in Mg-Al LDH. Simulated solid phase assemblages for NS-AS cements compared closely to the solid phases identified experimentally in these materials, and the simulations accurately predicted the experimentally measured chemical shrinkage in a NS-AS cement.

Phase diagrams for $(NH)_{0.5}$-AS- and NS-AS-based cements were simulated, which showed that C-(N-)A-S-H gel and MA-OH-LDH are formed over the majority of chemical compositions relevant to these cements. Natrolite and Ca-heulandite featured more prominently in the phase diagrams at lower CaO concentration, and higher SiO_2 and Al_2O_3 content, indicating that the bulk $CaO/(SiO_2 + Al_2O_3)$ ratio plays a significant role in stabilising zeolites, and therefore N-A-S(-H) gels, in AAS-based cements. Zeolites were predicted to be stable in NS-activated 75 mass% GBFS/25 mass% FA and MK cements but not in hybrid NS-activated 75 mass% GBFS/25 mass% PC. Therefore, these phase diagrams can be used as a reference tool for the development of high-performance AAS-based

cements, by enabling solid phase assemblages for these cements to be predicted from the bulk compositions of the raw materials used.

5. Acknowledgements

The authors thank the Faculty of Engineering, University of Sheffield, for funding and an anonymous reviewer who helped to improve the quality of the manuscript.

6. References

Allada, R., Navrotsky, A. and Boerio-Goates, J. (2005) Thermochemistry of hydrotalcite-like phases in the MgO-Al_2O_3-CO_2-H_2O system: a determination of enthalpy, entropy, and free energy. *Am. Mineral.* **90**, 329-335.

Andersen, M.D., Jakobsen, H.J. and Skibsted, J. (2006) A new aluminium-hydrate species in hydrated Portland cements characterized by ^{27}Al and ^{29}Si MAS NMR spectroscopy. *Cem. Concr. Res.* **36**, 3-17.

Anderson, G.M. and Crerar, D.A. (1993) *Thermodynamics in geochemistry: the equilibrium model*. Oxford University Press, Oxford.

Arthur, R., Sasamoto, H., Walker, C. and Yui, M. (2011) Polymer model of zeolite thermochemical stability. *Clays Clay Miner.* **59**, 626-639.

Atkins, M., Bennett, D.G., Dawes, A.C., Glasser, F.P., Kindness, A. and Read, D. (1992) A thermodynamic model for blended cements. *Cem. Concr. Res.* **22**, 497-502.

Babushkin, I., Matveev, G.M. and Mchedlow-Petrossyan, O.P. (1985) *Thermodynamics of silicates*. Springer-Verlag, Berlin.

Baerlocher, C., McCusker, L.B. and Olson, D.H. (2007) *Atlas of zeolite framework types*. Elsevier, Netherlands.

Bai, Y., Collier, N.C., Milestone, N.B. and Yang, C.H. (2011) The potential for using slags activated with near neutral salts as immobilisation matrices for nuclear wastes containing reactive metals. *J. Nucl. Mater.* **413**, 183-192.

776 Ben Haha, M., Le Saoût, G., Winnefeld, F. and Lothenbach, B. (2011a) Influence of activator type on
777 hydration kinetics, hydrate assemblage and microstructural development of alkali activated blast-
778 furnace slags. *Cem. Concr. Res.* **41**, 301-310.

779 Ben Haha, M., Lothenbach, B., Le Saoût, G. and Winnefeld, F. (2011b) Influence of slag chemistry
780 on the hydration of alkali-activated blast-furnace slag - part I: effect of MgO. *Cem. Concr. Res.* **41**,
781 955-963.

782 Ben Haha, M., Lothenbach, B., Le Saoût, G. and Winnefeld, F. (2012) Influence of slag chemistry on
783 the hydration of alkali-activated blast-furnace slag - part II: effect of Al_2O_3. *Cem. Concr. Res.* **42**, 74-
784 83.

785 Bennett, D.G., Read, D., Atkins, M. and Glasser, F.P. (1992) A thermodynamic model for blended
786 cements. II: cement hydrate phases; thermodynamic values and modelling studies. *J. Nucl. Mater.*
787 **190**, 315-325.

788 Bernal, S.A., Provis, J.L., Rose, V. and Mejía De Gutierrez, R. (2011) Evolution of binder structure in
789 sodium silicate-activated slag-metakaolin blends. *Cem. Concr. Compos.* **33**, 46-54.

790 Bernal, S.A., Provis, J.L., Brice, D.G., Kilcullen, A., Duxson, P. and van Deventer, J.S.J. (2012)
791 Accelerated carbonation testing of alkali-activated binders significantly underestimates service life:
792 the role of pore solution chemistry. *Cem. Concr. Res.* **42**, 1317-1326.

793 Bernal, S.A., Provis, J.L., Walkley, B., San Nicolas, R., Gehman, J.G., Brice, D.G., Kilcullen, A.,
794 Duxson, P. and van Deventer, J.S.J. (2013) Gel nanostructure in akali-activated binders based on slag
795 and fly ash, and effects of accelerated carbonation. *Cem. Concr. Res.* **53**, 127-144.

796 Bernal, S.A., Rose, V. and Provis, J.L. (2014a) The fate of iron in blast furnace slag particles during
797 alkali-activation. *Mater. Chem. Phys.* **146**, 1-5.

798 Bernal, S.A., San Nicolas, R., Myers, R.J., Mejía de Gutiérrez, R., Puertas, F., van Deventer, J.S.J.
799 and Provis, J.L. (2014b) MgO content of slag controls phase evolution and structural changes induced
800 by accelerated carbonation in alkali-activated binders. *Cem. Concr. Res.* **57**, 33-43.

801 Bernal, S.A., Provis, J.L., Myers, R.J., San Nicolas, R. and van Deventer, J.S.J. (2015) Role of
802 carbonates in the chemical evolution of sodium carbonate-activated slag binders. *Mater. Struct.* **48**,
803 517-529.

804 Bonk, F., Schneider, J., Cincotto, M.A. and Panepucci, H. (2003) Characterization by multinuclear
805 high-resolution NMR of hydration products in activated blast-furnace slag pastes. *J. Am. Ceram. Soc.*
806 **86**, 1712-1719.

807 Brough, A.R. and Atkinson, A. (2002) Sodium silicate-based, alkali-activated slag mortars - part I.
808 Strength, hydration and microstructure. *Cem. Concr. Res.* **32**, 865-879.

809 Burciaga-Díaz, O. and Escalante-García, J.I. (2013) Structure, mechanisms of reaction, and strength
810 of an alkali-activated blast-furnace slag. *J. Am. Ceram. Soc.* **96**, 3939-3948.

811 Bury, C.R. and Redd, R. (1933) The system sodium carbonate-calcium carbonate-water. *J. Chem.*
812 *Soc.*, 1160-1162.

813 Chen, W. and Brouwers, H.J.H. (2007) The hydration of slag, part 1: reaction models for alkali-
814 activated slag. *J. Mater. Sci.* **42**, 428-443.

815 Davidovits, J. (1991) Geopolymers - inorganic polymeric new materials. *J. Therm. Anal.* **37**, 1633-
816 1656.

817 de Wolff, P.M. (1952) The crystal structure of artinite, $Mg_2(OH)_2CO_3 \cdot 3H_2O$. *Acta Crystallogr.* **5**,
818 286-287.

819 Dickens, B. and Brown, W.E. (1969) Crystal structures of $CaNa_2(CO_3)_2 \cdot 5H_2O$, synthetic gaylussite,
820 and $CaNa_2(CO_3)_2 \cdot 2H_2O$, synthetic pirssonite. *Inorg. Chem.* **8**, 2093-2103.

821 Dilnesa, B.Z., Lothenbach, B., Renaudin, G., Wichser, A. and Kulik, D. (2014) Synthesis and
822 characterization of hydrogarnet $Ca_3(Al_xFe_{1-x})_2(SiO_4)_y(OH)_{4(3-y)}$. *Cem. Concr. Res.* **59**, 96-111.

823 Duxson, P., Fernandez-Jimenez, A., Provis, J.L., Lukey, G.C., Palomo, A. and van Deventer, J.S.J.
824 (2007) Geopolymer technology: the current state of the art. *J. Mater. Sci.* **42**, 2917-2933.

825 Dyson, H.M., Richardson, I.G. and Brough, A.R. (2007) A combined ^{29}Si MAS NMR and selective
826 dissolution technique for the quantitative evaluation of hydrated blast furnace slag cement blends. *J.*
827 *Am. Ceram. Soc.* **90**, 598-602.

828 Fyfe, C.A., Gobbi, G.C., Hartman, J.S., Klinowski, J. and Thomas, J.M. (1982) Solid-state magic-
829 angle spinning. Aluminum-27 nuclear magnetic resonance studies of zeolites using a 400-MHz high-
830 resolution spectrometer. *J. Phys. Chem.* **86**, 1247-1250.

831 Gao, W. and Li, Z. (2012) Solubility and K_{SP} of $Mg_4Al_2(OH)_{14} \cdot 3H_2O$ at the various ionic strengths.
832 *Hydrometallurgy* **117–118**, 36-46.

García-Lodeiro, I., Palomo, A., Fernández-Jiménez, A. and MacPhee, D.E. (2011) Compatibility studies between N-A-S-H and C-A-S-H gels. Study in the ternary diagram Na_2O-CaO-Al_2O_3-SiO_2-H_2O. *Cem. Concr. Res.* **41**, 923-931.

Glasser, F.P. and Atkins, M. (1994) Cements in radioactive waste disposal. *MRS Bull.* **19**, 33-38.

Graf, D.L. and Bradley, W.F. (1962) The crystal structure of huntite, $Mg_3Ca(CO_3)_4$. *Acta Crystallogr.* **15**, 238-242.

Gruskovnjak, A., Lothenbach, B., Holzer, L., Figi, R. and Winnefeld, F. (2006) Hydration of alkali-activated slag: comparison with ordinary Portland cement. *Adv. Cem. Res.* **18**, 119-128.

Helgeson, H.C., Delany, J.M. and Nesbitt, H.W. (1978) Summary and critique of the thermodynamic properties of rock-forming minerals. *Am. J. Sci.* **278-A**, 1-229.

Helgeson, H.C., Kirkham, D.H. and Flowers, G.C. (1981) Theoretical prediction of the thermodynamic behavior of aqueous electrolytes at high pressures and temperatures: IV. Calculation of activity coefficients, osmotic coefficients, and apparent molal and standard and relative partial molal properties to 600°C and 5 kb. *Am. J. Sci.* **281**, 1249-1516.

Hemingway, B.S. and Robie, R.A. (1972) The heat capacities at low temperatures and entropies at 298.15K of huntite, $CaMg_3(CO_3)_4$, and artinite, $Mg_2(OH)_2CO_3 \cdot 3H_2O$. *Am. Mineral.* **57**, 1754-1767.

Hill, R.J., Canterford, J.H. and Moyle, F.J. (1982) New data for lansfordite. *Mineral. Mag.* **46**, 453-457.

Hummel, W., Berner, U., Curti, E., Pearson, F.J. and Thoenen, T. (2002) *Nagra/PSI Chemical Thermodynamic Database 01/01*. Universal Publishers, Parkland, Florida.

Ismail, I., Bernal, S.A., Provis, J.L., San Nicolas, R., Hamdan, S. and van Deventer, J.S.J. (2014) Modification of phase evolution in alkali-activated blast furnace slag by the incorporation of fly ash. *Cem. Concr. Compos.* **45**, 125-135.

Jennings, H.M. (2008) Refinements to colloid model of C-S-H in cement: CM-II. *Cem. Concr. Res.* **38**, 275-289.

Jensen, O.M. and Hansen, P.F. (2001) Water-entrained cement-based materials - I. Principles and theoretical background. *Cem. Concr. Res.* **31**, 647-654.

860 Johnson, C.A. and Glasser, F.P. (2003) Hydrotalcite-like minerals ($M_2Al(OH)_6(CO_3)_{0.5}\cdot XH_2O$, where
861 M = Mg, Zn, Co, Ni) in the environment: synthesis, characterization and thermodynamic stability.
862 *Clays Clay Miner.* **51**, 1-8.

863 Johnson, G.K., Flotow, H.E. and O'Hare, P.A.G. (1982) Thermodynamic studies of zeolites; analcime
864 and dehydrated analcime. *Am. Mineral.* **67**, 736-748.

865 Johnson, G.K., Flotow, H.E., O'Hare, P.A.G. and Wise, W.S. (1983) Thermodynamic studies of
866 zeolites; natrolite, mesolite and scolecite. *Am. Mineral.* **68**, 1134-1145.

867 Johnson, J.W., Oelkers, E.H. and Helgeson, H.C. (1992) SUPCRT92: A software package for
868 calculating the standard molal thermodynamic properties of minerals, gases, aqueous species, and
869 reactions from 1 to 5000 bar and 0 to 1000°C. *Comput. Geosci.* **18**, 899-947.

870 Kiseleva, I., Navrotsky, A., Belitsky, I. and Fursenko, B. (2001) Thermochemical study of calcium
871 zeolites—heulandite and stilbite. *Am. Mineral.* **86**, 448-455.

872 Königsberger, E., Königsberger, L.-C. and Gamsjäger, H. (1999) Low-temperature thermodynamic
873 model for the system Na_2CO_3−$MgCO_3$−$CaCO_3$−H_2O. *Geochim. Cosmochim. Acta* **63**, 3105-3119.

874 Kulik, D.A. and Kersten, M. (2001) Aqueous solubility diagrams for cementitious waste stabilization
875 systems: II. End-member stoichiometries of ideal calcium silicate hydrate solid solutions. *J. Am.*
876 *Ceram. Soc.* **84**, 3017-3026.

877 Kulik, D.A. (2011) Improving the structural consistency of C-S-H solid solution thermodynamic
878 models. *Cem. Concr. Res.* **41**, 477-495.

879 Kulik, D.A., Wagner, T., Dmytrieva, S.V., Kosakowski, G., Hingerl, F.F., Chudnenko, K.V. and
880 Berner, U. (2013) GEM-Selektor geochemical modeling package: revised algorithm and GEMS3K
881 numerical kernel for coupled simulation codes. *Comput. Geosci.* **17**, 1-24.

882 Le Saoût, G., Ben Haha, M., Winnefeld, F. and Lothenbach, B. (2011) Hydration degree of alkali-
883 activated slags: a ^{29}Si NMR study. *J. Am. Ceram. Soc.* **94**, 4541-4547.

884 Lothenbach, B. and Winnefeld, F. (2006) Thermodynamic modelling of the hydration of Portland
885 cement. *Cem. Concr. Res.* **36**, 209-226.

886 Lothenbach, B. and Gruskovnjak, A. (2007) Hydration of alkali-activated slag: thermodynamic
887 modelling. *Adv. Cem. Res.* **19**, 81-92.

888 Lothenbach, B., Matschei, T., Möschner, G. and Glasser, F.P. (2008) Thermodynamic modelling of
889 the effect of temperature on the hydration and porosity of Portland cement. *Cem. Concr. Res.* **38**, 1-
890 18.

891 Lothenbach, B. (2010) Thermodynamic equilibrium calculations in cementitious systems. *Mater.*
892 *Struct.* **43**, 1413-1433.

893 Lothenbach, B., Pelletier-Chaignat, L. and Winnefeld, F. (2012) Stability in the system $CaO–Al_2O_3–$
894 H_2O. *Cem. Concr. Res.* **42**, 1621-1634.

895 Matschei, T., Lothenbach, B. and Glasser, F.P. (2007) Thermodynamic properties of Portland cement
896 hydrates in the system $CaO\text{-}Al_2O_3\text{-}SiO_2\text{-}CaSO_4\text{-}CaCO_3\text{-}H_2O$. *Cem. Concr. Res.* **37**, 1379-1410.

897 McLellan, B.C., Williams, R.P., Lay, J., van Riessen, A. and Corder, G.D. (2011) Costs and carbon
898 emissions for geopolymer pastes in comparison to ordinary portland cement. *J. Cleaner Prod.* **19**,
899 1080-1090.

900 Moloy, E.C., Liu, Q. and Navrotsky, A. (2006) Formation and hydration enthalpies of the
901 hydrosodalite family of materials. *Micropor. Mesopor. Mat.* **88**, 283-292.

902 Monnin, C. and Schott, J. (1984) Determination of the solubility products of sodium carbonate
903 minerals and an application to trona deposition in Lake Magadi (Kenya). *Geochim. Cosmochim. Acta*
904 **48**, 571-581.

905 Morimoto, K., Anraku, S., Hoshino, J., Yoneda, T. and Sato, T. (2012) Surface complexation
906 reactions of inorganic anions on hydrotalcite-like compounds. *J. Colloid Interf. Sci.* **384**, 99-104.

907 Möschner, G., Lothenbach, B., Rose, J., Ulrich, A., Figi, R. and Kretzschmar, R. (2008) Solubility of
908 Fe–ettringite ($Ca_6[Fe(OH)_6]_2(SO_4)_3\cdot 26H_2O$). *Geochim. Cosmochim. Acta* **72**, 1-18.

909 Möschner, G., Lothenbach, B., Winnefeld, F., Ulrich, A., Figi, R. and Kretzschmar, R. (2009) Solid
910 solution between Al-ettringite and Fe-ettringite ($Ca_6[Al_{1-x}Fe_x(OH)_6]_2(SO_4)_3\cdot 26H_2O$). *Cem. Concr.*
911 *Res.* **39**, 482-489.

912 Muller, A.C.A., Scrivener, K.L., Gajewicz, A.M. and McDonald, P.J. (2013) Use of bench-top NMR
913 to measure the density, composition and desorption isotherm of C–S–H in cement paste. *Micropor.*
914 *Mesopor. Mat.* **178**, 99-103.

915 Myers, R.J., Bernal, S.A., San Nicolas, R. and Provis, J.L. (2013) Generalized structural description
916 of calcium-sodium aluminosilicate hydrate gels: the cross-linked substituted tobermorite model.
917 *Langmuir* **29**, 5294-5306.

Myers, R.J., Bernal, S.A. and Provis, J.L. (2014) A thermodynamic model for C-(N-)A-S-H gel: CNASH_ss. Derivation and application. *Cem. Concr. Res.* **66**, 27-47.

Myers, R.J., Bernal, S.A., Provis, J.L., Gehman, J.D. and van Deventer, J.S.J. (2015a) The role of Al in cross-linking of alkali-activated slag cements. *J. Am. Ceram. Soc.* **98**, 996-1004.

Myers, R.J., L'Hôpital, E., Provis, J.L. and Lothenbach, B. (2015b) Effect of temperature and aluminium on calcium aluminosilicate hydrate chemistry under equilibrium conditions. *Cem. Concr. Res.* **68**, 83-93.

Provis, J.L., Lukey, G.C. and van Deventer, J.S.J. (2005) Do geopolymers actually contain nanocrystalline zeolites? A reexamination of existing results. *Chem. Mater.* **17**, 3075-3085.

Provis, J.L., Myers, R.J., White, C.E., Rose, V. and van Deventer, J.S.J. (2012) X-ray microtomography shows pore structure and tortuosity in alkali-activated binders. *Cem. Concr. Res.* **42**, 855-864.

Provis, J.L. (2014) Geopolymers and other alkali activated materials: why, how, and what? *Mater. Struct.* **47**, 11-25.

Provis, J.L. and Bernal, S.A. (2014) Geopolymers and related alkali-activated materials. *Annu. Rev. Mater. Res.* **44**, 299-327.

Puertas, F., Palacios, M., Manzano, H., Dolado, J.S., Rico, A. and Rodríguez, J. (2011) A model for the C-A-S-H gel formed in alkali-activated slag cements. *J. Eur. Ceram. Soc.* **31**, 2043-2056.

Richardson, I.G. and Groves, G.W. (1993) The incorporation of minor and trace elements into calcium silicate hydrate (C-S-H) gel in hardened cement pastes. *Cem. Concr. Res.* **23**, 131-138.

Richardson, I.G., Brough, A.R., Groves, G.W. and Dobson, C.M. (1994) The characterization of hardened alkali-activated blast-furnace slag pastes and the nature of the calcium silicate hydrate (C-S-H) phase. *Cem. Concr. Res.* **24**, 813-829.

Richardson, I.G. (2004) Tobermorite/jennite- and tobermorite/calcium hydroxide-based models for the structure of C-S-H: applicability to hardened pastes of tricalcium silicate, β-dicalcium silicate, Portland cement, and blends of Portland cement with blast-furnace slag, metakaolin, or silica fume. *Cem. Concr. Res.* **34**, 1733-1777.

Richardson, I.G. (2013) Clarification of possible ordered distributions of trivalent cations in layered double hydroxides and an explanation for the observed variation in the lower solid-solution limit. *Acta Crystallogr. B.* **69**, 629-633.

948 Robie, R.A. and Hemingway, B.S. (1995) *Thermodynamic properties of minerals and related*
949 *substances at 298.15 K and 1 bar (10^5 Pascals) pressure and at higher temperatures*. United States
950 Government Printing Office, Washington D.C.

951 Rozov, K. (2010) Stability and solubility of hydrotalcite-pyroaurite solid solutions: synthesis,
952 characterization and thermodynamic modelling, *Department of Science*. Ph.D. Thesis, The University
953 of Bern, Bern.

954 Rozov, K.B., Berner, U., Kulik, D.A. and Diamond, L.W. (2011) Solubility and thermodynamic
955 properties of carbonate-bearing hydrotalcite-pyroaurite solid solutions with a 3:1 Mg/(Al+Fe) mole
956 ratio. *Clays Clay Miner.* **59**, 215-232.

957 Sakulich, A.R., Anderson, E., Schauer, C. and Barsoum, M.W. (2009) Mechanical and
958 microstructural characterization of an alkali-activated slag/limestone fine aggregate concrete. *Constr.*
959 *Build. Mater.* **23**, 2951-2957.

960 Sakulich, A.R., Miller, S. and Barsoum, M.W. (2010) Chemical and microstructural characterization
961 of 20-month-old alkali-activated slag cements. *J. Am. Ceram. Soc.* **93**, 1741-1748.

962 Savage, D., Soler, J.M., Yamaguchi, K., Walker, C., Honda, A., Inagaki, M., Watson, C., Wilson, J.,
963 Benbow, S., Gaus, I. and Rueedi, J. (2011) A comparative study of the modelling of cement hydration
964 and cement–rock laboratory experiments. *Appl. Geochem.* **26**, 1138-1152.

965 Schmidt, T., Lothenbach, B., Romer, M., Scrivener, K., Rentsch, D. and Figi, R. (2008) A
966 thermodynamic and experimental study of the conditions of thaumasite formation. *Cem. Conc. Res.*
967 **38**, 337-349.

968 Schneider, J., Cincotto, M.A. and Panepucci, H. (2001) ^{29}Si and ^{27}Al high-resolution NMR
969 characterization of calcium silicate hydrate phases in activated blast-furnace slag pastes. *Cem. Concr.*
970 *Res.* **31**, 993-1001.

971 Shi, C., Krivenko, P.V. and Roy, D. (2006) *Alkali-Activated Cements and Concretes*, 1st ed. Taylor &
972 Francis, New York.

973 Shock, E.L., Helgeson, H.C. and Sverjensky, D.A. (1989) Calculation of the thermodynamic and
974 transport properties of aqueous species at high pressures and temperatures: standard partial molal
975 properties of inorganic neutral species. *Geochim. Cosmochim. Acta* **53**, 2157-2183.

976 Shock, E.L. and Helgeson, H.C. (1990) Calculation of the thermodynamic and transport properties of
977 aqueous species at high pressures and temperatures: Standard partial molal properties of organic
978 species. *Geochim. Cosmochim. Acta* **54**, 915-945.

979 Shock, E.L., Sassani, D.C., Willis, M. and Sverjensky, D.A. (1997) Inorganic species in geologic
980 fluids: correlations among standard molal thermodynamic properties of aqueous ions and hydroxide
981 complexes. *Geochim. Cosmochim. Acta* **61**, 907-950.

982 Snellings, R. (2013) Solution-controlled dissolution of supplementary cementitious material glasses at
983 pH 13: the effect of solution composition on glass dissolution rates. *J. Am. Ceram. Soc.* **96**, 2467-
984 2475.

985 Sun, G.K., Young, J.F. and Kirkpatrick, R.J. (2006) The role of Al in C-S-H: NMR, XRD, and
986 compositional results for precipitated samples. *Cem. Concr. Res.* **36**, 18-29.

987 Sverjensky, D.A., Shock, E.L. and Helgeson, H.C. (1997) Prediction of the thermodynamic properties
988 of aqueous metal complexes to 1000°C and 5 kb. *Geochim. Cosmochim. Acta* **61**, 1359-1412.

989 Taga, T. (1969) Crystal structure of $Na_2CO_3 \cdot 10H_2O$. *Acta Crystallogr. B* **25**, 2656-2658.

990 Taylor, R., Richardson, I.G. and Brydson, R.M.D. (2010) Composition and microstructure of 20-year-
991 old ordinary Portland cement-ground granulated blast-furnace slag blends containing 0 to 100% slag.
992 *Cem. Concr. Res.* **40**, 971-983.

993 Tazawa, E.-i., Miyazawa, S. and Kasai, T. (1995) Chemical shrinkage and autogenous shrinkage of
994 hydrating cement paste. *Cem. Concr. Res.* **25**, 288-292.

995 Thoenen, T. and Kulik, D.A. (2003) *Nagra/PSI chemical thermodynamic database 01/01 for the*
996 *GEM-Selektor (V.2-PSI) geochemical modeling code*. Paul Scherrer Institute, Villigen; available at
997 http://gems.web.psi.ch/TDB/doc/pdf/TM-44-03-04-web.pdf.

998 Thoenen, T., Hummel, W. and Berner, U. (2013) The PSI/Nagra Chemical Thermodynamic Database
999 12/07: present status and future developments. *Mineral. Mag.* **77**, 2327.

1000 Thomas, J.J., Allen, A.J. and Jennings, H.M. (2012) Density and water content of nanoscale solid C-
1001 S-H formed in alkali-activated slag (AAS) paste and implications for chemical shrinkage. *Cem.*
1002 *Concr. Res.* **42**, 377-383.

1003 van Deventer, J.S.J., Provis, J.L. and Duxson, P. (2012) Technical and commercial progress in the
1004 adoption of geopolymer cement. *Miner. Eng.* **29**, 89-104.

Wagman, D.D., Evans, W.H., Parker, V.B., Schumm, R.H. and Halow, I. (1982) *The NBS tables of chemical thermodynamic properties: selected values for inorganic and C_1 and C_2 organic substances in SI units*. American Chemical Society and the American Institute of Physics for the National Bureau of Standards, New York.

Wagner, T., Kulik, D.A., Hingerl, F.F. and Dmytrieva, S.V. (2012) GEM-Selektor geochemical modeling package: TSolMod library and data interface for multicomponent phase models. *Can. Mineral.* **50**, 1173-1195.

Wang, S.D. and Scrivener, K.L. (1995) Hydration products of alkali activated slag cement. *Cem. Concr. Res.* **25**, 561-571.

Wolery, T.J., Jove-Colon, C.F., Krumhansl, J.L., Spencer, R.E., Brady, P.V. and Freeze, G.A. (2007) Qualification of thermodynamic data for geochemical modeling of mineral-water interactions in dilute systems. Sandia National Laboratories, United States, p. 412.